Hygrothermal analysis of magneto-electro-elastic plate using 3D finite element analysis

M. Vinyas, S.C. Kattimani *

Department of Mechanical Engineering, National Institute of Technology Karnataka, Surathkal 575025, India

ARTICLE INFO

ABSTRACT

In this article, the static response of magneto-electro-elastic (MEE) plate subjected to hygrothermal loads is investigated using the finite element (FE) method. A FE formulation is derived using the principle of total potential energy and linear coupled constitutive equations of MEE materials by taking into account the thermal and hygroscopic field effects. A uniform temperature rise and moisture concentration rise has been considered. The variations of static parameters are estimated along the MEE plate length by considering the temperature and moisture dependant elastic stiffness coefficients. The coupled FE equilibrium equations in terms of displacements, electric and magnetic potentials are solved directly using condensation procedure. Numerical examples of the FE results are presented and discussed in detail to understand the significant effects of hygrothermal loading, temperature and moisture dependent material properties, boundary conditions and aspect ratio on the direct (displacements, electric potential and magnetic potential) and derived quantities (stresses, electric displacement and magnetic flux density) of MEE plate.

1. Introduction

Most recently, the multifunctional capabilities of the smart structures composed of magneto-electro-elastic (MEE) composites have attracted the interest of many researchers. These composite materials are capable of converting energy from one form to another. In addition, MEE composites exhibit coupling between electric, magnetic and elastic material properties which are many times larger than the individual phase [1]. Thus, it offers a great opportunity to tailor a wide range of coupled material properties and provides a greater scope to design efficient intelligent structures used in automotive and aerospace industries. More often, a factual performance of these intelligent structures throughout its service life is expected in various environmental and loading conditions. Hence, the accurate prediction of the coupled response of MEE structures subjected to various multifield loads such as hygrothermal loads, magnetic load, electric loads and mechanical fields are highly significant. In specific, understanding the behavior of these multifunctional materials under hygrothermal environment is an important issue and demands further investigation.

The new era of smart structures evolved with the development of the functionally graded materials (FGM). Realizing the impor-

tance of these materials and its potentiality to adapt itself in thermal environment, many researchers evaluated the response of FGM smart structures under thermal load. The different plate theories were proposed in order to evaluate the thermoelastic bending response of FGM sandwich plates subjected to thermal gradients [2–4]. The thermal buckling behavior of FGM sandwich plates was interpreted by Bourada et al. [5] with the aid of four variable refined plate theory. Apart from FGM plates, the axisymmetric structures like FGM cylinders and FGM spheres have a considerable practical interest in many thermal engineering applications. Wang [6] analysed the piezothermoelastic behavior of smart sandwich cylindrical structure subjected to steady state temperature field. Saadatfar and Rastgoo [7] and Saadatfar and Razavi [8] investigated the thermal bending response of radially polarized piezoelectric hollow sphere and piezoelectric hollow cylinder, respectively. Saadatfar and Khafri [9–11] studied the thermoelastic problem of a long and short length FGM hollow cylinder bonded to functionally graded piezoelectric material (FGPM) layers in a constant magnetic field. Also, few researchers have studied the static behavior of FGM cylindrical shell with piezoelectric layers (FGPM) perfectly bonded to its surface [12–16]. The results presented in their study has paved way for the clear understanding of the coupled thermo-electro-elastic response FGM cylindrical shells subjected to thermal loads.

Moreover, the external moisture concentration together with the high temperature may degrade the performance of the smart

* Corresponding author.
E-mail address: sck@nitk.ac.in (S.C. Kattimani).

structure with its prolonged utilization. Many works have been reported in the literature which emphasizes the significance of examining the combined effect of moisture and thermal fields (hygrothermal effects) on the laminated composites, FGM, FGPM and piezoelectric structures. Brischetto [17] investigated the hygrothermoelastic static behavior of multilayered composite and sandwich shells using a refined two-dimensional model. Some of the specific studies discuss the free vibration and bending response of the composite structures in hygrothermal environment [18–21]. Zidi et al. [22] studied the influence of hygrothermal loads on the bending response of FG plate resting on elastic foundation. In many practical situations, the hazardous hygrothermal environment conditions results in imperfect bonding of the laminates. Hence, addressing the behavior of imperfectly bonded laminated structures is critical. In this regard, Saadatfar and Khafri [23,24] analysed the effect of axisymmetric hygrothermal loads on a rotating FGM cylindrical shell with imperfectly surface bounded FGPM. They also evaluated the influence of elastic foundation. More recently, considering the effect of constant magnetic field, Saadatfar [25] investigated the multiphysics response of FGM cylindrical shell with imperfect surface bounded FGPM subjected to hygrothermo-electro mechanical loads.

Meanwhile, for piezoelectric materials, the externally applied hygrothermal loads results in the development of electrical polarization along with the mechanical displacement in the uncoupled

hygrothermopiezoelectricity analysis. Hence, the coupled analysis dealing with the multiphysics phenomenon of hygrothermo-piezoelectricity is considered to be prominent due to mutual coupling of moisture, temperature, electric and elastic fields [26,27]. Smittakaron and Heyliger [28] developed a three-dimensional discrete layer model to evaluate the static and transient behavior of a laminated hygrothermo-piezoelectric plate by. Raja et al. [29] proposed a coupled piezoelectric finite element (FE) formulation and investigated the influence of active stiffness on the dynamic response of hygrothermo-piezoelectric laminates. They extended their study to analyse the bending response of piezo-hygrothermo-elastic flat and curved plates with active control [30]. Kerur and Ghosh [31] derived a FE formulation for a hygrothermo-electro-mechanical coupled problem. Zenkour [32] obtained an analytical solution and described the hygrothermal responses in inhomogeneous piezoelectric hollow cylinders.

In the recent years, apart from FGM and piezoelectric material, MEE materials have received much attention, as a novel kind of intelligent materials. The fascinating and improved magnetoelectric coupling displayed by the MEE materials has justified its extensive usage in numerous smart structures. The fully coupled analysis of multiphase, functionally graded and layered MEE composites has been carried out in many investigations. The free vibration behavior of MEE structures was analysed using various techniques like exact solution method, discrete layer approximate method, state vector method, finite element method etc. [33–39]. The active control of geometrically nonlinear vibrations of MEE plates, FG-MEE plates and doubly curved MEE shells has been dealt by Kattimani and Ray [40–42]. It is evident from the literature that an abundant research is devoted to study the static behavior [43–49] and buckling behavior [50–52] of MEE structures. In addition, Carrera et al. [53] extended the unified formulation and developed a FE based on Reissner's Mixed Variational Theorem (RMVT), to investigate the influence of MEE fields on the coupled response of multilayered plates. Using the layer wise and equivalent single
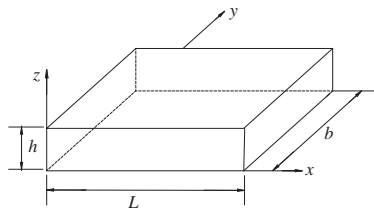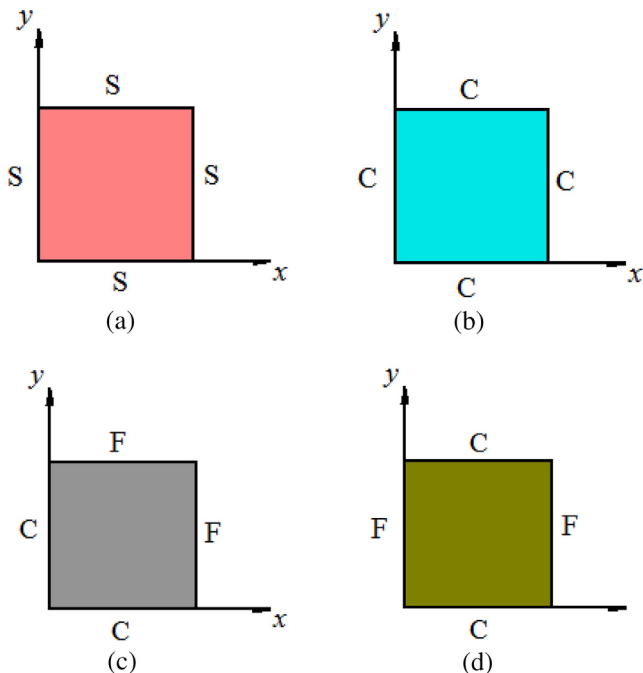

Fig. 1. MEE plate geometry.

Fig. 2. Schematic of various boundary condition of MEE plate (a) all sides simply supported (*SSSS*) (b) all sides clamped (*CCCC*) (c) adjacent sides clamped (*CFFC*) (d) opposite sides clamped (*FCFC*).

Table 1
Material properties of 60% BaTiO$_3$ and CoFe$_2$O$_4$ and adaptive wood made of BaTiO$_3$ and CoFe$_2$O$_4$.

Material property	Material constants	0.6 V_f (Kondaiah et al.[59]	Adaptive wood (Akbarzadeh et al.[63])
Elastic constants (GPa)	$C_{11} = C_{22}$	200	286
	C_{12}	110	173
	$C_{13} = C_{23}$	110	170.5
	C_{33}	190	269.5
	$C_{44} = C_{55}$	45	45.3
	C_{66}	45	56.5
Piezoelectric constants (C/m^2)	e_{31}	−3.5	−4.4
	e_{33}	11	18.6
	e_{15}	0	11.6
Dielectric constant (10^{-9} C^2/Nm^2)	$\varepsilon_{11} = \varepsilon_{22}$	0.9	0.08
	ε_{33}	7.5	0.093
Magnetic permeability (10^{-4} Ns^2/C^2)	$\mu_{11} = \mu_{22}$	−1.5	−5.9
	μ_{33}	0.75	1.57
Piezomagnetic constants (N/Am)	q_{31}	200	580
	q_{33}	260	700
	q_{15}	180	560
Magneto-electric constant (10^{-12} Ns/VC)	$m_{11} = m_{22}$	6	0
	m_{33}	2500	3
Pyroelectric constant (10^{-5} C/m^2 K)	p_2	−12.4	−13
Pyromagnetic constant (10^{-3} C/m^2 K)	τ_2	5.92	6
Thermal expansion coefficient (10^{-6} K^{-1})	$\alpha_1 = \alpha_2$	12.9	14.1
	α_3	7.8	7.2
Moisture expansion coefficient (m^3 kg^{-1})	β_1	–	0
	$\beta_2 = \beta_3$	–	1.1×10^{-4}
Density (kg/m^3)	ρ	5600	5300

layer plate model the static and free vibration behavior of MEE multilayered plates was investigated by Milazzo [54] and Benedetti and Milazzo [55].

Literatures reveal that the MEE structures under thermal environment exhibit considerable changes in the mechanical behavior due to additional coupling of thermal field with the remaining coupled fields. Sunar [56] demonstrated the coupled behavior of thermopiezomagnetic continuum with the aid of FE formulation. Ootao and Tanigawa [57] developed an exact solution for the transient behavior of multilayered magneto-thermo-electro-elastic (MTEE)

strip subjected to non uniform and unsteady heating. Kumaravel et al. [58] studied the influence of both uniform and non-uniform load on the static behavior of MEE beam. Further, limited works have been reported on the influence of pyroeffects on the static behavior of MEE structures in thermal environment. Among them, Kondaiah et al. [59,60] investigated the static behavior of MEE beams and plates under uniform thermal load. Recently, Vinyas and Kattimani [61,62] investigated the coupled behavior of stepped functionally graded (SFG) and multiphase MEE beam subjected to different thermal loads.
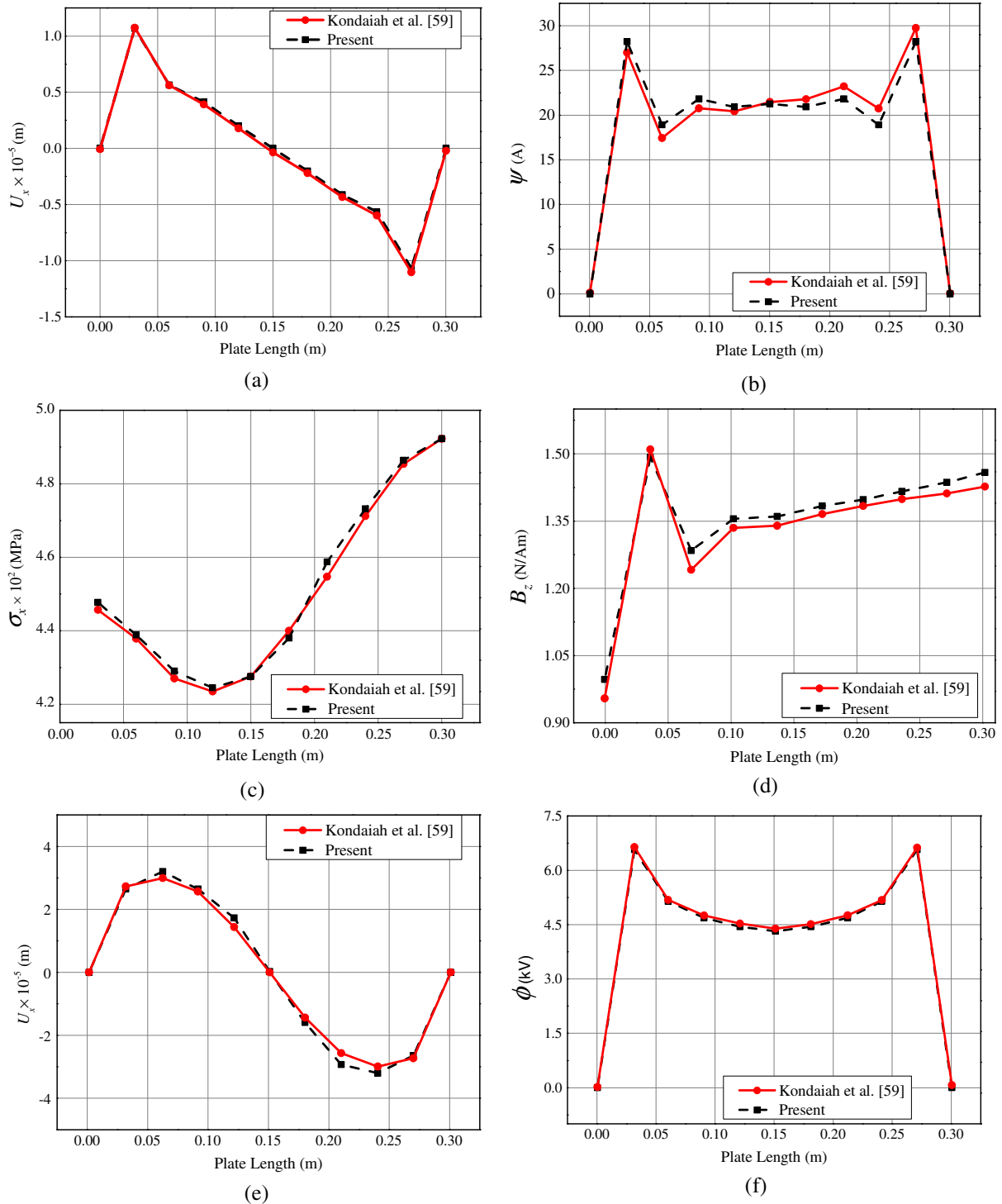

Fig. 3. Validation plots (a) displacement component in *x*-direction U_x for *CCCC* MEE plate (b) magnetic potential of *CCCC* MEE plate (c) normal stress σ_x of *CFFC* MEE plate (d) magnetic flux density B_z of *CFFC* MEE plate (e) displacement component in *x*-direction U_x of *FCFC* MEE plate (f) electric potential of *FCFC* MEE plate.

The study on hygrothermo-magneto-electro-elastic response of MEE structure is still an overlooked area. Only few pioneers have attempted to investigate the response of MEE structures subjected to hygrothermal loads. Among them, the influence of hygrothermal loads on MEE behavior of rotating cylinders was analysed by Akbarzadeh and Chen [63] considering the temperature and moisture dependent material properties. They presented an analytical solution and evaluated the hygrothermal stresses in one-dimensional functionally graded piezoelectric media [64]. Saadatfar and Khafri [65] evaluated the hygrothermo-magneto-electro-elastic behavior of FG-MEE hollow sphere resting on elastic foundation. Akbarzadeh and Pasini [66] presented a closed form solutions to analyse the steady state responses of multilayered and FG infinitely long cylinders and thin circular disks subjected to hygrothermal loading.

From the comprehensive literature review, it may be observed that no work has been reported on the static analysis of MEE plates in hygrothermal environment. Further, to the best of authors' knowledge, it appears from the literature that there is no FE formulation available for the investigation of the direct and derived quantities of MEE plates subjected to hygrothermal loads. Hence, the present work aims to develop a FE formulation to analyse the multiphysics characteristics of hygrothermo-magneto-electro-elastic plates. The equilibrium equations in terms of moisture concentration, temperature distribution, displacement, magnetic potential and electric potential are solved using condensation procedure. Numerical examples are presented to illustrate the influence of hygrothermal loading, temperature and moisture dependent elastic stiffness coefficients, different boundary conditions and aspect ratios on the static behavior of MEE plates.

2. Basic formulation of the problem

2.1. Problem description

A schematic representation of a multiphase magneto-electro-elastic (MEE) plate referred to a Cartesian co-ordinate with the *x*, *y* and *z* coordinates spanning its length *L*, width *b* and thickness *h*, respectively, is shown in Fig. 1. The MEE plate is loaded hygrothermally with a uniform temperature rise of ΔT and a moisture concentration change of Δm. The commonly used plate configurations considered for the analysis are illustrated in Fig. 2(a)–(d).

The constraints corresponding to the different boundary conditions are given as follows:

Clamped edge (C) : $U_x = U_v = U_w = \phi = \psi = 0$ (1.a)

Free edge (F) : $U_x = U_v = U_w = \phi = \psi \neq 0$ (1.b)

Simply supported edge (S) :

$U_x \neq 0; U_v = U_w = \phi = \psi = 0$ at $x = 0, L$ (1.c)

$U_v \neq 0;$ $U_x = U_w = \phi = \psi = 0$ at $y = 0, b$

2.2. Constitutive equations

The linear coupled constitutive equations of a magneto-electro-elastic (MEE) material considering hygrothermal fields can be represented as follows:

$$\{\sigma\} = [C]\{\varepsilon\} - [e]\{E\} - [q]\{H\} - \{\lambda\} - \{\gamma\} \tag{2.a}$$

$$\{D\} = [e]^T\{\varepsilon\} + [\eta]\{E\} + [m]\{H\} + \{p\}\Delta T + \{\chi\}\Delta m \tag{2.b}$$

$$\{B\} = [q]^T\{\varepsilon\} + [m]\{E\} + [\mu]\{H\} + \{\tau\}\Delta T + \{\upsilon\}\Delta m \tag{2.c}$$

$$\{\lambda\} = [C]\{\alpha\}\Delta T \tag{2.d}$$

$$\{\gamma\} = [C]\{\xi\}\Delta m \tag{2.e}$$

where, $\{\lambda\}$ is the thermal stress developed due to change in temperature, $\{\gamma\}$ corresponds to the hygroscopic stresses developed due to change in moisture concentration; $[C]$, $[e]$, $[q]$, $\{\alpha\}$ and $\{\xi\}$ are the elastic co-efficient matrix, piezoelectric coefficient matrix, magnetostrictive coefficient matrix, thermal expansion co-efficient vector and moisture expansion coefficient vector, respectively; $[\eta]$, $[m]$, $\{p\}$, $\{\tau\}$, $[\mu]$, $\{\chi\}$ and $\{\upsilon\}$ are the dielectric constant matrix, electromagnetic coefficient matrix, pyroelectric coefficient vector, pyromagnetic coefficient vector, magnetic permeability constant matrix, hygroelectric coefficient vector and hygromagnetic coefficient vector, respectively; $\{\sigma\}$, $\{D\}$ and $\{B\}$ represent the stress tensor, electric displacement vector and the magnetic flux vector, respectively; $\{\varepsilon\}$, $\{E\}$, $\{H\}$ are the linear strain tensor, electric field vector, magnetic field vector, respectively; ΔC and ΔT are the moisture concentration rise from stress free reference concentration and temperature rise from the stress-free reference temperature, respectively.

2.3. Finite element (FE) formulation

The FE model of the MEE plate is discretized using eight noded 3D isoparametric brick element. Each element is assumed to have five degrees of freedom *viz.* three translational, one electric (ϕ) and magnetic potential (ψ). The translational displacement vector associated with the *i*th ($i = 1, 2, 3,\ldots,8$) node of the element can be expressed as

$$\{d_{ti}\} = [U_{xi} U_{vi} U_{wi}]^T \tag{3}$$

At any point within the element, the displacement vector $\{d_t\}$, electric potential vector $\{\phi\}$ and magnetic potential vector $\{\psi\}$ can be represented in terms of the nodal displacement vector $\{d_t^e\}$, the nodal electric potential vector $\{\phi^e\}$ and the nodal magnetic potential vector $\{\psi^e\}$, respectively, as follows:

$$\{d_t\} = [N_t]\{d_t^e\}, \{\phi\} = [N_\phi]\{\phi^e\}, \{\psi\} = [N_\psi]\{\psi^e\} \tag{4}$$

The various nodal vectors appearing in Eq. (4) can be represented as

$$\begin{aligned}
&\{d_t^e\} = [\{d_{t1}\}^T \{d_{t2}\}^T \ldots \{d_{t8}\}^T]^T, \quad \{\phi^e\} = [\phi_1 \phi_2 \ldots \phi_8]^T, \\
&\{\psi^e\} = [\psi_1 \psi_2 \ldots \psi_8]^T, \\
&[N_t] = [N_{t1} N_{t2} \ldots N_{t8}] \quad, N_{ti} = n_i I_t, \quad [N_\phi] = [n_1 n_2 \ldots n_8], \\
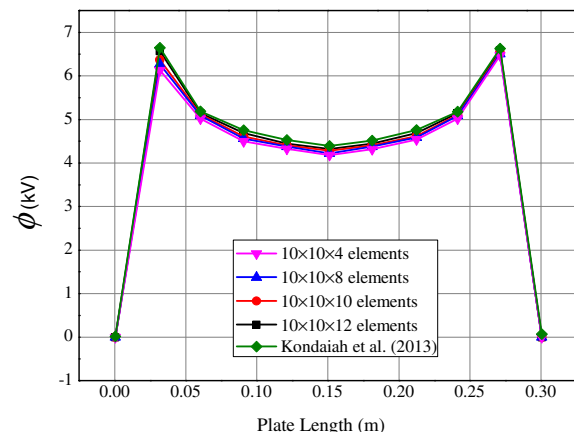&[N_\psi] = [n_1 n_2 \ldots n_8]
\end{aligned} \tag{5}$$

Fig. 4. Convergence of electric potential ϕ for *FCFC* MEE plate.

where, n_i is the natural coordinate shape function associated with the ith node of the element; I_t is the identity matrix; $[N_t]$,$[N_\phi]$ and $[N_\psi]$ are (3×24), (1×8) and (1×8) shape function matrices, respectively. The shape functions for the eight noded isoparametric element in the natural co-ordinate (ξ, η, ζ) are given by

$$N_1 = \tfrac{1}{8}(1 - \xi)(1 - \eta)(1 - \zeta), \quad N_2 = \tfrac{1}{8}(1 + \xi)(1 - \eta)(1 - \zeta),$$
$$N_3 = \tfrac{1}{8}(1 + \xi)(1 + \eta)(1 - \zeta),$$
$$N_4 = \tfrac{1}{8}(1 - \xi)(1 + \eta)(1 - \zeta), \quad N_5 = \tfrac{1}{8}(1 - \xi)(1 - \eta)(1 + \zeta), \quad (6)$$
$$N_6 = \tfrac{1}{8}(1 + \xi)(1 - \eta)(1 + \zeta),$$
$$N_7 = \tfrac{1}{8}(1 + \xi)(1 + \eta)(1 + \zeta), \quad N_8 = \tfrac{1}{8}(1 - \xi)(1 + \eta)(1 + \zeta)$$
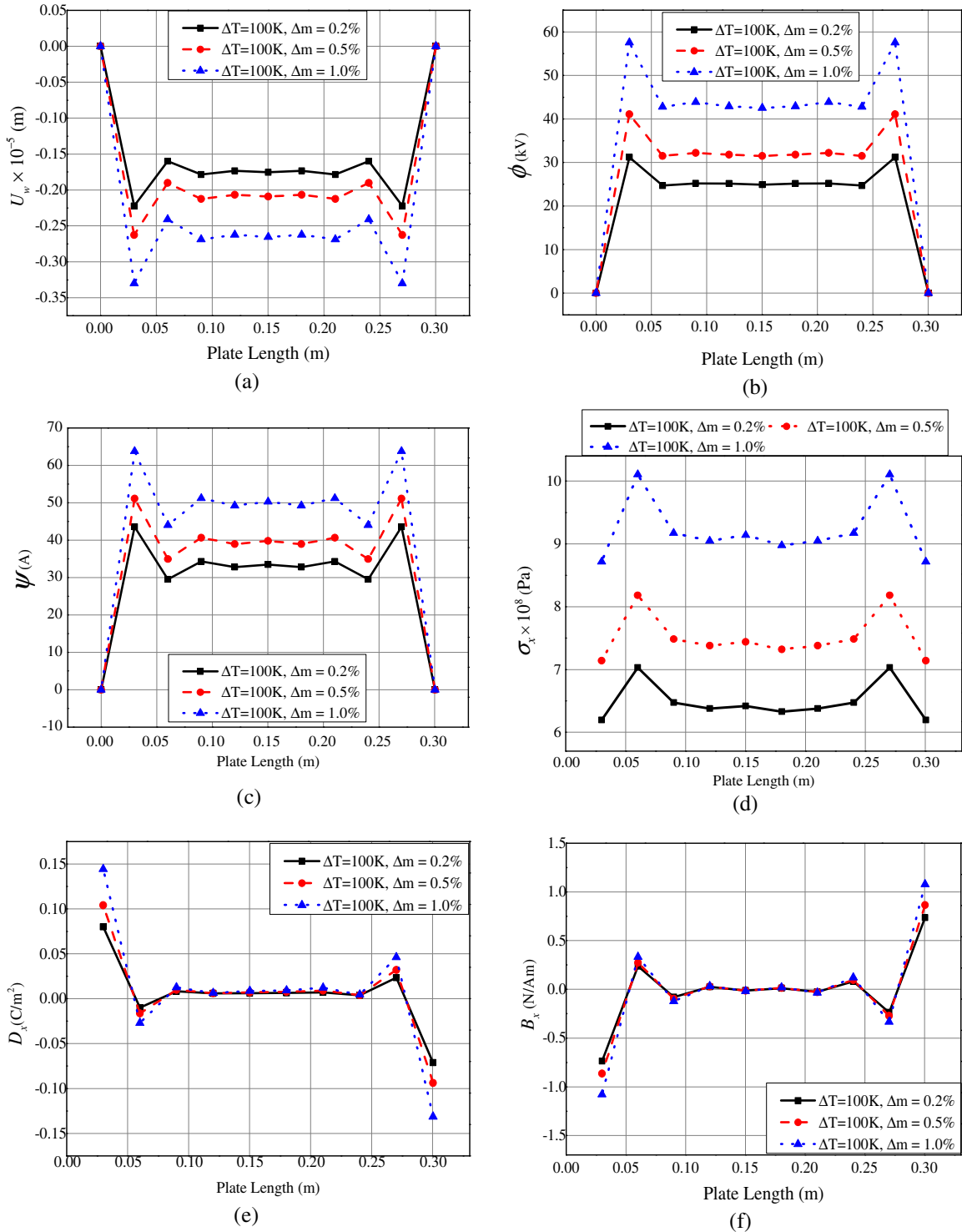

Fig. 5. Effect of hygrothermal load on (a) displacement component U_w (b) electric potential ϕ (c) magnetic potential ψ (d) normal stress σ_x (e) electric displacement component D_x (f) magnetic flux density B_x.

As the elastic waves propagate several orders of magnitude slower than the electromagnetic ones, the approximation of quasi static electro-magnetic behavior is assumed (Benedetti and Milazzo 2017). Therefore, the electric intensity (E) and magnetic intensity (H) can be related to gradients of the scalar electric potential (ϕ) and magnetic potential (ψ), respectively, as follows:

$$\{E\} = \begin{Bmatrix} E_x \\ E_y \\ E_z \end{Bmatrix} = \begin{Bmatrix} -\frac{\partial \phi}{\partial x} \\ -\frac{\partial \phi}{\partial y} \\ -\frac{\partial \phi}{\partial z} \end{Bmatrix} \tag{7.a}$$

$$\{H\} = \begin{Bmatrix} H_x \\ H_y \\ H_z \end{Bmatrix} = \begin{Bmatrix} -\frac{\partial \psi}{\partial x} \\ -\frac{\partial \psi}{\partial y} \\ -\frac{\partial \psi}{\partial z} \end{Bmatrix} \tag{7.b}$$

The strain vector $\{\varepsilon\}$, electric potential vector $\{\phi\}$ and magnetic potential vector $\{\psi\}$ of the system can be related to the nodal displacement vector $\{d_t^e\}$, nodal electric potential vector $\{\phi^e\}$ and nodal magnetic potential vector $\{\psi^e\}$, respectively, with the aid of the derivative of shape function matrices as follows:

$$\begin{aligned} \{\varepsilon\} &= [L_t][N_t]\{d_t^e\} = [B_t]\{d_t^e\} \\ \{H\} &= [L_\psi][N_\psi]\{\psi^e\} = [B_\psi]\{\psi^e\} \\ \{E\} &= [L_\phi][N_\phi]\{\phi^e\} = [B_\phi]\{\phi^e\} \end{aligned} \tag{8}$$

in which,

$$[L_t] = \begin{bmatrix} \frac{\partial}{\partial x} & 0 & 0 \\ 0 & \frac{\partial}{\partial y} & 0 \\ 0 & 0 & \frac{\partial}{\partial z} \\ 0 & \frac{\partial}{\partial z} & \frac{\partial}{\partial y} \\ \frac{\partial}{\partial z} & 0 & \frac{\partial}{\partial x} \\ \frac{\partial}{\partial y} & \frac{\partial}{\partial x} & 0 \end{bmatrix};$$

$$[N_t] = \begin{bmatrix} n_1 & 0 & 0 & n_2 & 0 & 0 & n_3 & 0 & 0 & \cdots & n_8 & 0 & 0 \\ 0 & n_1 & 0 & 0 & n_2 & 0 & 0 & n_3 & 0 & \cdots & 0 & n_8 & 0 \\ 0 & 0 & n_1 & 0 & 0 & n_2 & 0 & 0 & n_3 & \cdots & 0 & 0 & n_8 \end{bmatrix}$$

$$[L_\psi] = \begin{bmatrix} -\frac{\partial}{\partial x} \\ -\frac{\partial}{\partial y} \\ -\frac{\partial}{\partial z} \end{bmatrix}; \quad [N_\psi] = [cccn_1 \quad n_2 \quad n_3 \cdots n_8] \quad [L_\phi N_\phi] = [L_\psi N_\psi] \tag{9}$$

The shape function derivative matrices appearing in Eq. (8) can be written as

$$[B_t] = [B_{t1} B_{t2} \ldots B_{t8}], [B_\psi] = [B_{\psi 1} B_{\psi 2} \ldots B_{\psi 8}], \quad [B_\phi] = [B_{\phi 1} B_{\phi 2} \ldots B_{\phi 8}] \tag{10}$$

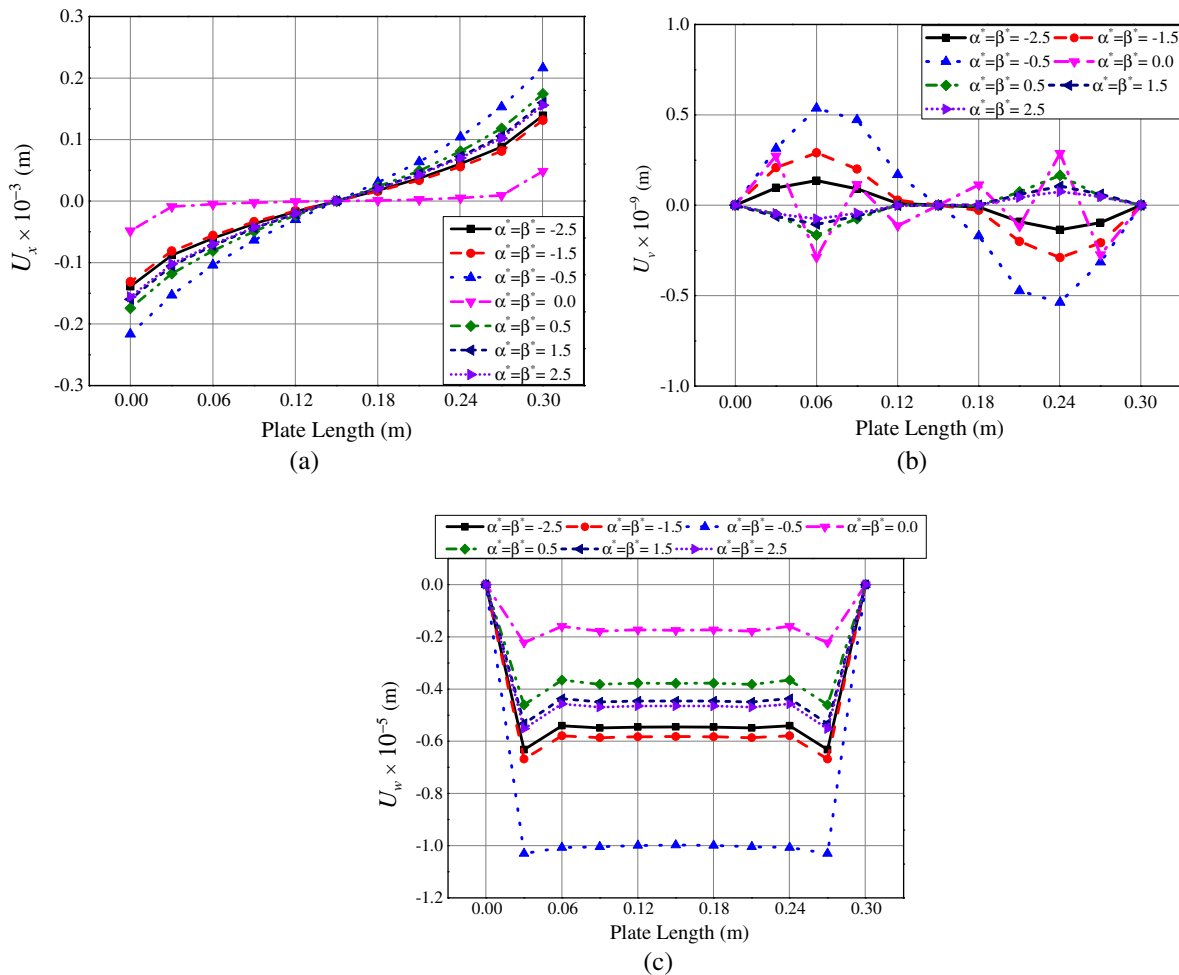in which, the sub matrices, $[B_{ti}]$, $[B_{\psi i}]$ and $[B_{\phi i}]$ are given by

Fig. 6. Effect of empirical constants on (a) displacement component U_x (b) displacement component U_v (c) transverse displacement component U_w of *SSSS* MEE plate.

$$[B_{ti}] = \begin{bmatrix} \frac{\partial n_i}{\partial x} & 0 & 0 \\ 0 & \frac{\partial n_i}{\partial y} & 0 \\ 0 & 0 & \frac{\partial n_i}{\partial z} \\ 0 & \frac{\partial n_i}{\partial z} & \frac{\partial n_i}{\partial y} \\ \frac{\partial n_i}{\partial z} & 0 & \frac{\partial n_i}{\partial x} \\ \frac{\partial n_i}{\partial y} & \frac{\partial n_i}{\partial x} & 0 \end{bmatrix}, \quad [B_{\psi i}] = \begin{bmatrix} \frac{-\partial n_i}{\partial x} \\ \frac{-\partial n_i}{\partial y} \\ \frac{-\partial n_i}{\partial z} \end{bmatrix}, \quad [B_{\phi i}] = \begin{bmatrix} \frac{-\partial n_i}{\partial x} \\ \frac{-\partial n_i}{\partial y} \\ \frac{-\partial n_i}{\partial z} \end{bmatrix} \quad (11)$$

where, $i = 1, 2, 3, \ldots, 8$ represents the node number. The derivatives of the shape functions n_i with respect to global coordinates (x, y and z) are expressed in terms of their derivatives with respect to ξ, η and ζ as follows:

$$\begin{Bmatrix} \frac{\partial n_i}{\partial x} \\ \frac{\partial n_i}{\partial y} \\ \frac{\partial n_i}{\partial z} \end{Bmatrix} = [J]^{-1} \begin{Bmatrix} \frac{\partial n_i}{\partial \xi} \\ \frac{\partial n_i}{\partial \eta} \\ \frac{\partial n_i}{\partial \zeta} \end{Bmatrix} \quad (12)$$

where, $[J]$ is the Jacobian matrix

$$[J] = \begin{bmatrix} \frac{\partial x}{\partial \xi} & \frac{\partial y}{\partial \xi} & \frac{\partial z}{\partial \xi} \\ \frac{\partial x}{\partial \eta} & \frac{\partial y}{\partial \eta} & \frac{\partial z}{\partial \eta} \\ \frac{\partial x}{\partial \zeta} & \frac{\partial y}{\partial \zeta} & \frac{\partial z}{\partial \zeta} \end{bmatrix} \quad (13)$$

2.4. Equations of motion

The governing equations of MEE plate in hygrothermal environment is derived by employing the principle of total potential energy [61] as follows:

$$T_p = \frac{1}{2}\left[\int_\Omega \{\varepsilon\}^T\{\sigma\}d\Omega - \int_\Omega \{E\}^T\{D\}d\Omega - \int_\Omega \{H\}^T\{B\}d\Omega\right]$$
$$- \int_A \{d_t\}^T\{f\}dA - \int_A \phi Q^\phi dA - \int_A \psi Q^\psi dA \quad (14)$$

where, $\{f\}$ is the traction force vector acting over an area A. The entire volume of the domain is represented by Ω. The surface electric charge density and surface magnetic charge density are represented by Q^ϕ and Q^ψ, respectively. The total potential energy is minimized by setting the first variation of Eq. (14) to zero.
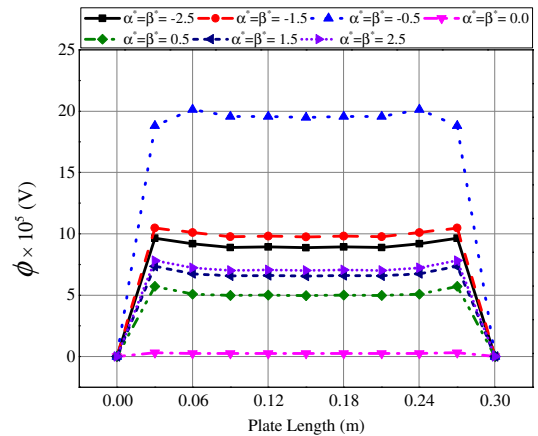
$$T_p = \frac{1}{2}\left[\int_\Omega \delta\{\varepsilon\}^T\{\sigma\}d\Omega - \int_\Omega \delta\{E\}^T\{D\}d\Omega - \int_\Omega \delta\{H\}^T\{B\}d\Omega\right]$$
$$- \int_A \delta\{d_t\}^T\{f\}dA - \int_A \delta\{\phi\}Q^\phi dA - \int_A \delta\{\psi\}Q^\psi dA = 0 \quad (15)$$
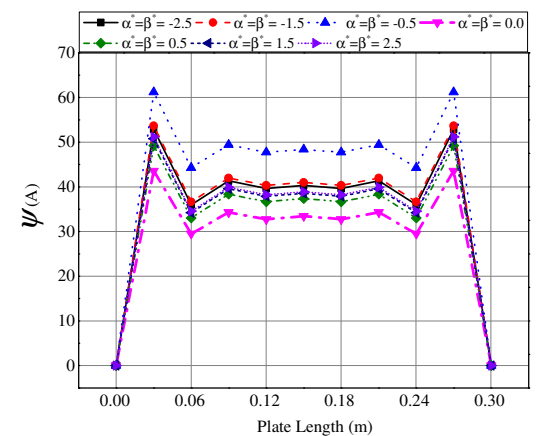
Substituting Eq. (2) into Eq. (15), we get,

$$T_p = \frac{1}{2}\int_\Omega \delta\{\varepsilon\}^T[C]\{\varepsilon\}d\Omega - \frac{1}{2}\int_\Omega \delta\{\varepsilon\}^T[e]\{E\}d\Omega$$
$$- \frac{1}{2}\int_\Omega \delta\{\varepsilon\}^T[q]\{H\}d\Omega - \frac{1}{2}\int_\Omega \delta\{\varepsilon\}^T[C]\{\alpha\}\Delta Td\Omega$$
$$- \frac{1}{2}\int_\Omega \delta\{\varepsilon\}^T[C]\{\xi\}\Delta md\Omega - \frac{1}{2}\int_\Omega \delta\{E\}^T[e]^T\{\varepsilon\}d\Omega$$
$$- \frac{1}{2}\int_\Omega \delta\{E\}^T[\eta]^T\{E\}d\Omega - \frac{1}{2}\int_\Omega \delta\{E\}^T[m]^T\{H\}d\Omega$$
$$- \frac{1}{2}\int_\Omega \delta\{E\}^T\{p\}\Delta Td\Omega - \frac{1}{2}\int_\Omega \delta\{E\}^T\{\chi\}\Delta md\Omega$$
$$- \frac{1}{2}\int_\Omega \delta\{H\}^T[q]^T\{\varepsilon\}d\Omega - \frac{1}{2}\int_\Omega \delta\{H\}^T[m]\{E\}d\Omega$$
$$- \frac{1}{2}\int_\Omega \delta\{H\}^T[\mu]\{H\}d\Omega - \frac{1}{2}\int_\Omega \delta\{H\}^T\{\tau\}\Delta Td\Omega$$
$$- \frac{1}{2}\int_\Omega \delta\{H\}^T\{\upsilon\}\Delta md\Omega - \int_A \delta\{d_t\}^T\{f\}dA$$
$$- \int_A \delta\{\phi\}Q^\phi dA - \int_A \delta\{\psi\}Q^\psi dA = 0 \quad (16)$$

Now, substituting Eq. (8) in Eq. (16), and assigning the coupled stiffness matrices for the various terms, we obtain Eq. (17) as follows:

$$T_p^e = \frac{1}{2}\left[\int_\Omega \delta\{d_t^e\}^T[K_{tt}^e]\{d_t^e\}d\Omega - \int_\Omega \delta\{d_t^e\}^T[K_{t\phi}^e]\{\phi^e\}d\Omega\right.$$
$$\left. - \int_\Omega \delta\{d_t^e\}^T[K_{t\psi}^e]\{\psi^e\}d\Omega - \frac{1}{2}\left[\int_\Omega \delta\{d_t^e\}^T\{F_{th}^e\}d\Omega\right.\right.$$
$$\left. - \int_\Omega \delta\{d_t^e\}^T\{F_{hy}^e\}d\Omega - \int_\Omega \delta\{\phi^e\}^T[K_{t\phi}^e]^T\{d_t^e\}d\Omega\right]$$
$$- \frac{1}{2}\left[\int_\Omega \delta\{\phi^e\}^T[K_{\phi\phi}^e]\{\phi^e\}d\Omega - \int_\Omega \delta\{\phi^e\}^T[K_{\phi\psi}^e]\{\psi^e\}d\Omega\right]$$
$$- \int_\Omega \delta\{\phi^e\}^T\{Fp.e^e\}d\Omega - \frac{1}{2}\left[\int_\Omega \delta\{\phi^e\}^T\{F_{h.e}^e\}d\Omega\right.$$
$$\left. - \int_\Omega \delta\{\psi^e\}^T[K_{t\psi}^e]^T\{dt^e\}d\Omega - \int_\Omega \delta\{\psi^e\}^T[K_{\phi\psi}^e]^T\{\phi^e\}d\Omega\right]$$
$$- \frac{1}{2}\left[\int_\Omega \delta\{\psi^e\}^T[K_{\psi\psi}^e]\{\psi^e\}d\Omega - \int_\Omega \delta\{\psi^e\}^T\{Fp.m^e\}d\Omega\right]$$
$$- \int_\Omega \delta\{\psi^e\}^T\{F_{h.m}^e\}d\Omega\right] - \int_A \delta\{d_t^e\}^T\{F_m^e\}dA$$
$$- \int_A \delta\{\phi^e\}\{F_\phi^e\}dA - \int_A \delta\{\psi^e\}\{F_\psi^e\}dA = 0 \quad (17)$$

(a)

(b)

Fig. 7. Effect of empirical constants on (a) electric potential ϕ (b) magnetic potential ψ of *SSSS* MEE plate.

Grouping the terms based on the coefficients of $\{d_t^e\}^T$, $\{\phi^e\}^T$ and $\{\psi^e\}^T$, Eq. (17) can be rearranged as follows:

$$[K_{tt}^e]\{d_t^e\} + [K_{t\phi}^e]\{\phi^e\} + [K_{t\psi}^e]\{\psi^e\} = \{F_m^e\} + \{F_{th}^e\} + \{F_{hy}^e\}$$

$$[K_{t\phi}^e]^T\{d_t^e\} - [K_{\phi\phi}^e]\{\phi^e\} - [K_{\phi\psi}^e]\{\psi^e\} = \{F_\phi^e\} - \{F_{p.e}^e\} - \{F_{h.e}^e\}$$

$$[K_{t\psi}^e]^T\{d_t^e\} - [K_{\phi\psi}^e]^T\{\phi^e\} - [K_{\psi\psi}^e]\{\psi^e\} = \{F_\psi^e\} - \{F_{p.m}^e\} - \{F_{h.m}^e\} \tag{18}$$

The various elemental stiffness matrices appearing in Eq. (18) are the elemental elastic stiffness matrix $[K_{tt}^e]$, the elemental electro-elastic coupling stiffness matrix $[K_{t\phi}^e]$, the elemental magneto-elastic coupling stiffness matrix $[K_{t\psi}^e]$, the elemental electric stiffness matrix $[K_{\phi\phi}^e]$, the elemental magnetic stiffness matrix $[K_{\psi\psi}^e]$, the elemental electro-magnetic stiffness matrix $[K_{\phi\psi}^e]$. The various elemental load vectors are the elemental mechanical load vector $\{F_m^e\}$, the elemental thermal load vector $\{F_{th}^e\}$, the elemental hygroscopic load vector $\{F_{hy}^e\}$, the elemental hygro-electric load vector $\{F_{h.e}^e\}$, the elemental hygro-magnetic load vector $\{F_{h.m}^e\}$, the elemental electric charge load vector $\{F_\phi^e\}$, the elemental magnetic current load vector $\{F_\psi^e\}$, the elemental pyroelectric load vector $\{F_{p.e}^e\}$, the elemental pyromagnetic load vector $\{F_{p.m}^e\}$. The explicit forms of these matrices and load vectors are given as follows:

$$[K_{tt}^e] = \int_\Omega [B_t]^T[C][B_t]d\Omega, \ [K_{t\phi}^e] = \int_\Omega [B_t]^T[e][B_\phi]d\Omega,$$

$$[K_{t\psi}^e] = \int_\Omega [B_t]^T[q][B_\psi]d\Omega,$$

$$[K_{\phi\phi}^e] = \int_\Omega [B_\phi]^T[\eta][B_\phi]d\Omega, \ [K_{\phi\psi}^e] = \int_\Omega [B_\phi]^T[m][B_\psi]d\Omega,$$

$$[K_{\psi\psi}^e] = \int_\Omega [B_\psi]^T[\mu][B_\psi]d\Omega$$

$$\{F_m^e\} = \int_A [N_t]^T fdA, \ \{F_\phi^e\} = \int_A [N_\phi]^T Q^\phi dA,$$

$$\{F_\psi^e\} = \int_A [N_\psi]^T Q^\psi dA \ \{F_{th}^e\} = \int_\Omega [B_t]^T[C]\{\alpha\}\Delta Td\Omega,$$

$$\{F_{hy}^e\} = \int_\Omega [B_t]^T[C]\{\xi\}\Delta md\Omega,$$

$$\{Fp.e^e\} = \int_\Omega [B_\phi]^T\{p\}\Delta Td\Omega \ \{F_{h.e}^e\} = \int_\Omega [B_\phi]^T\{\chi\}\Delta md\Omega,$$

$$\{F_{p.m}^e\} = \int_\Omega [B_\psi]^T\{\tau\}\Delta Td\Omega$$

$$\{F_{h.m}^e\} = \int_\Omega [B_\psi]^T\{\upsilon\}\Delta md\Omega \tag{19}$$

In the absence of mechanical load $\{F_m^e\}$, elemental electric charge load $\{\phi^e\}$ and elemental magnetic current $\{\psi^e\}$, the elemental equations of motion is globalised in a straight forward manner to obtain the global equations of motion as follows:

$$[K_{tt}^g]\{d_t\} + [K_{t\phi}^g]\{\phi\} + [K_{t\psi}^g]\{\psi\} = \{F_{th}^g\} + \{F_{hy}^g\} \tag{20.a}$$

$$[K_{t\phi}^g]^T\{d_t\} - [K_{\phi\phi}^g]\{\phi\} - [K_{\phi\psi}^g]\{\psi\} = \{F_{p.e}^g\} + \{F_{h.e}^g\} \tag{20.b}$$

$$[K_{t\psi}^g]^T\{d_t\} - [K_{\phi\psi}^g]^T\{\phi\} - [K_{\psi\psi}^g]\{\psi\} = \{F_{p.m}^g\} + \{F_{h.m}^g\} \tag{20.c}$$
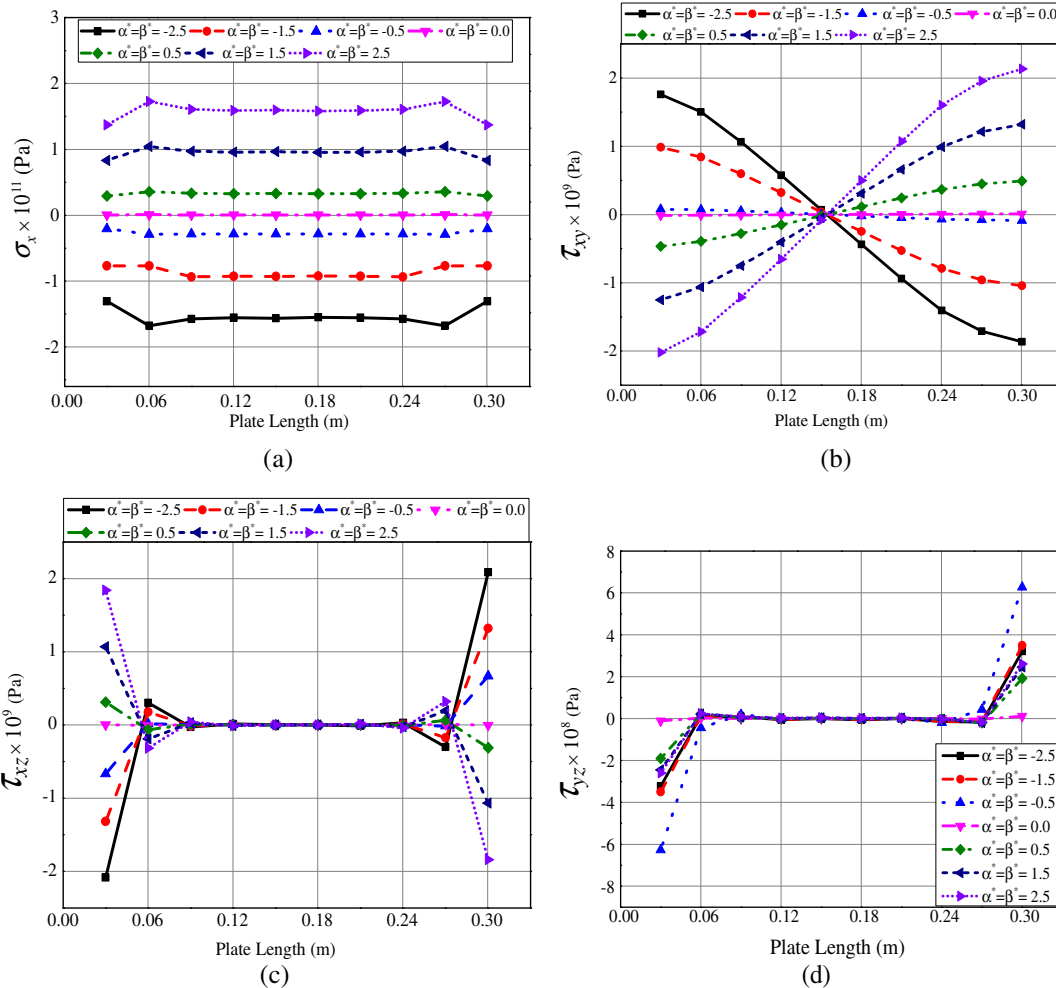

Fig. 8. Effect of empirical constants on (a) normal stress σ_x (b) shear stress τ_{xy} (c) shear stress τ_{xz} (d) shear stress τ_{yz} of *SSSS* MEE plate.

where, different global stiffness matrices in Eq. (20) are the global elastic stiffness matrix $[K_{tt}^g]$, the global electro-elastic coupling stiffness matrix $[K_{t\phi}^g]$, the global magneto-elastic coupling stiffness matrix $[K_{t\psi}^g]$, the global electric stiffness matrix $[K_{\phi\phi}^g]$, the global magnetic stiffness matrix $[K_{\psi\psi}^g]$, the global electro-magnetic stiffness matrix $[K_{\phi\psi}^g]$. The various global load vectors are the global mechanical load vector $\{F_m^g\}$, the global thermal load vector $\{F_{th}^g\}$, the global hygroscopic load vector $\{F_{hy}^g\}$, the global hygro-electric load vector $\{F_{h.e}^g\}$, the global hygro-magnetic load vector $\{F_{h.m}^g\}$, the global electric charge load vector $\{F_\phi^g\}$, the global magnetic current load vector $\{F_\psi^g\}$, the global pyroelectric load vector $\{F_{p.e}^g\}$, the global pyromagnetic load vector $\{F_{p.m}^g\}$.

Using the condensation approach, Eq. (20) is solved to obtain the nodal displacements generated due to hygrothermal loading, which is back substituted to determine the nodal electric and magnetic potential. The other fields viz. $\{\sigma\}$, $\{D\}$ and $\{B\}$ are calculated by post computations through constitutive equations. From Eq. (20.c), solving for $\{\psi\}$ we obtain

$$\{\psi\} = [K_{\psi\psi}^g]^{-1}[[K_{t\psi}^g]^T\{d_t\} - [K_{\phi\psi}^g]^T\{\phi\} - \{\{F_{p.m}^g\} + \{F_{h.m}^g\}\}] \quad (21.a)$$

Solving Eq. (21.a) in Eq. (20.b) and solving for $\{\phi\}$, we obtain

$$\{\phi\} = [K_2]^{-1}[K_1]\{d_t\} - [K_2]^{-1}\{F_{\phi\_sol}\} \quad (21.b)$$

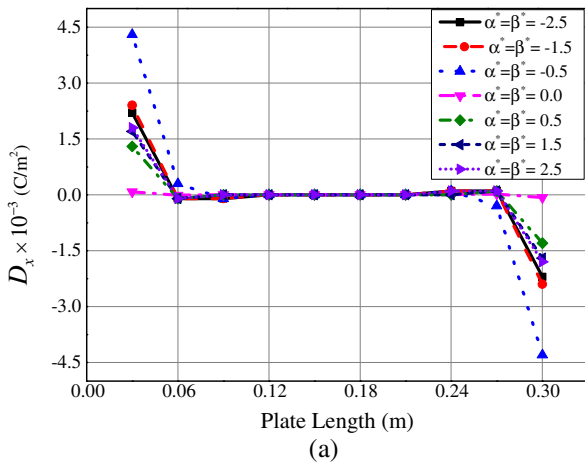Consequently, on substituting Eq. (21.a) and Eq. (21.b), the Eq. (20.a) can be modified as

$$[K_{eq}]\{d_t\} = \{F_{eq}\} \quad (22)$$

The explicit form of the global various stiffness matrices [Keq] and force vectors appearing in Eqs. (21) and (22) are given as follows:
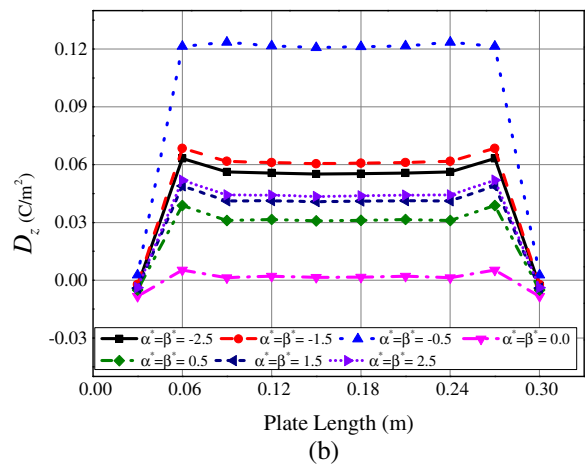
$$[K_{eq}] = [K_7], [K_9] = [K_{t\psi}^g][K_{\psi\psi}^g]^{-1} - [K_6][K_4], [K_8] = [K_6][K_2]^{-1},$$

$$[K_7] = [K_5] + [K_6][K_3],$$

$$[K_6] = [K_{t\phi}^g] - [K_{t\psi}^g][K_{\psi\psi}^g]^{-1}[K_{\phi\psi}^g], [K_5] = [K_{tt}^g] + [K_{t\psi}^g][K_{\psi\psi}^g]^{-1}[K_{\psi t}^g],$$

$$[K_4] = [K_2]^{-1}[K_{\psi\phi}^g][K_{\psi\psi}^g], [K_3] = [K_2]^{-1}[K_1],$$

$$[K_2] = [K_{\phi\phi}^g] - [K_{\psi\phi}^g][K_{\psi\psi}^g]^{-1}[K_{\phi\psi}^g],$$

$$[K_1] = [K_{\phi t}^g] - [K_{\psi\phi}^g][K_{\psi\psi}^g]^{-1}[K_{\psi t}^g], [K_{1\_\psi}] = [K_{\psi t}^g] - [K_{\phi\psi}^g][K_3],$$

$$[K_{2\_\psi}] = [K_{\psi\psi}^g]^{-1}[K_{\phi\psi}^g][K_2]^{-1},$$

$$[K_{3\_\psi}] = [K_{\psi\psi}^g]^{-1}[K_{\phi\psi}^g][K_2]^{-1}[K_{\psi\phi}^g]^T[K_{\psi\psi}^g]^{-1} + [K_{\psi\psi}^g]^{-1}$$

$$\{F_{eq}\} = [K_9][\{F_{p.m}^g\} + \{F_{h.m}^g\}] + [K_8][\{F_{p.e}^g\} + \{F_{h.e}^g\}] + [\{F_{th}^g\} + \{F_{hy}^g\}],$$

$$\{F_{\phi\_sol}\} = [\{F_{p.e}^g\} + \{F_{h.e}^g\}] - [K_{\psi\phi}^g]^T[K_{\psi\psi}^g]^{-1}[\{F_{p.m}^g\} + \{F_{h.m}^g\}]$$

$$(23)$$

3. Numerical results and discussions

The finite element (FE) formulation derived in the preceding section is used to demonstrate the static behavior of MEE plates under hygrothermal loading. The material properties of the adap-
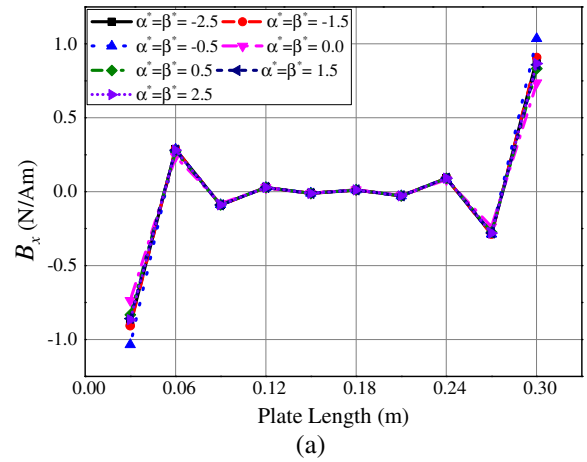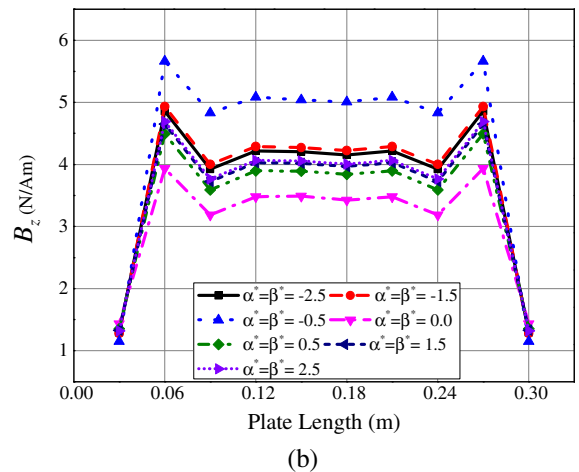

Fig. 9. Effect of empirical constants on electric displacement components (a) D_x (b) D_z of *SSSS* MEE plate.

Fig. 10. Effect of empirical constants on magnetic flux density components (a) B_x (b) B_z of *SSSS* MEE plate.

tive wood made of BaTiO$_3$ and CoFe$_2$O$_4$ [63] tabulated in Table 1 are used in the analysis. The geometrical dimensions of the MEE plate considered for the analysis are the length of the plate $L = 0.3$ m, width $b = 0.3$ m and the thickness $h = 0.006$ m. The variation of direct quantities (displacements and potentials) and derived quantities (stresses, electric displacement and magnetic flux density) are evaluated along the plate length. In addition, the influence of temperature and moisture dependent elastic stiffness coefficients, different boundary conditions and aspect ratios, on the static parameters of a multiphase MEE plate is also analysed through the numerical illustrations. The assumed temperature (T) and moisture (m) boundary conditions can be written as follows:
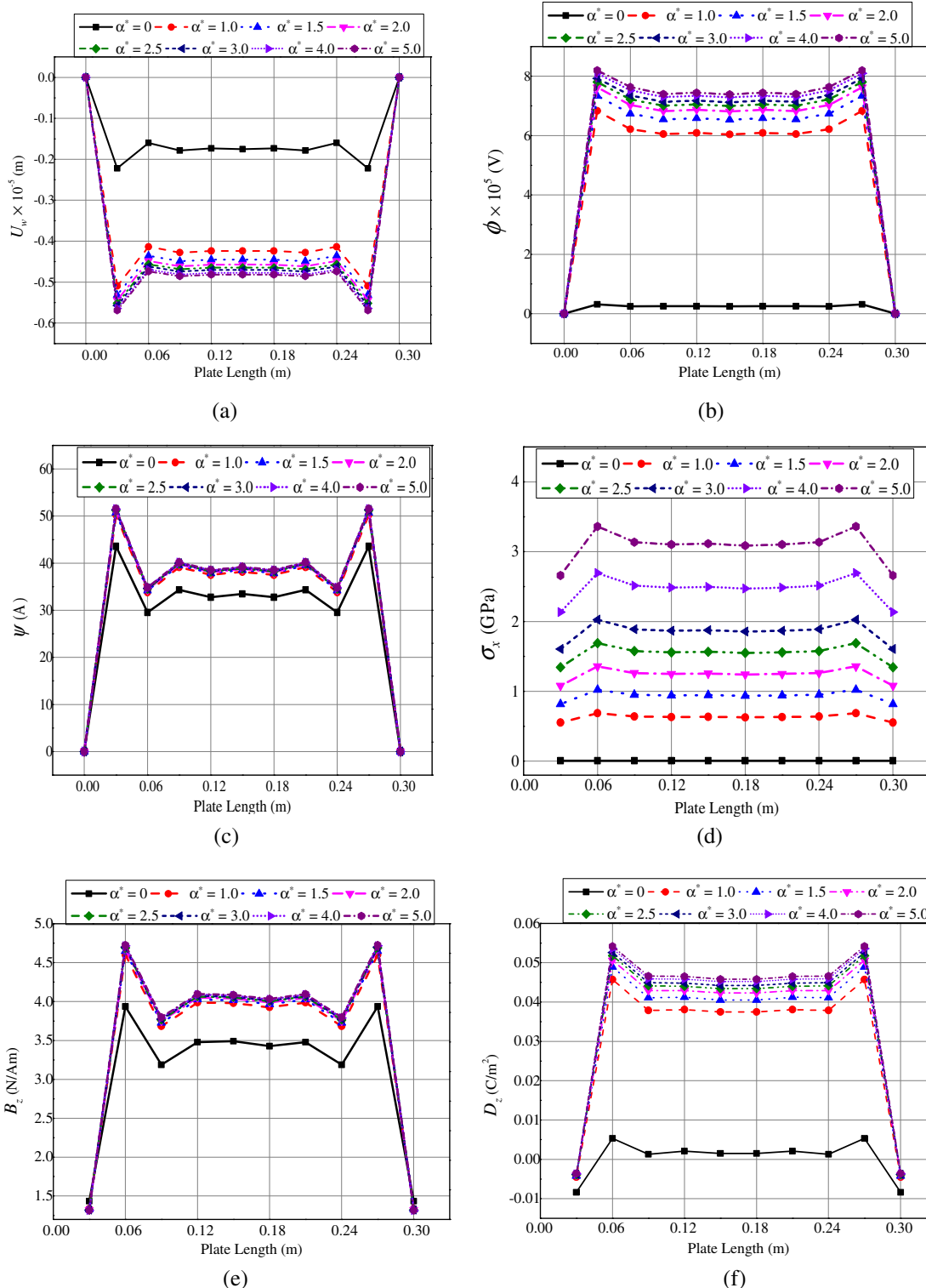

Fig. 11. Influence of α^* on (a) displacement component U_w (b) electric potential ϕ (c) magnetic potential ψ (d) normal stress σ_x (e) magnetic flux density B_z (f) electric displacement D_z.

$$T(x,0) = 0; \quad T(x,b) = 0; \quad T(0,b) = 0; \quad T(L,y) = 0;$$
$$T(x,y,z) = T_{uni}$$
$$m(x,0) = 0; \quad m(x,b) = 0; \quad m(0,b) = 0; \quad m(L,y) = 0; \quad (24)$$
$$m(x,y,z) = m_{uni}$$

in which, T_{uni} and m_{uni} are the uniform temperature and uniform moisture concentrations considered for the study.

3.1. Validation of the FE formulation

It is noteworthy, to mention at this point that no work has been reported on the static behavior of MEE plates under hygrothermal loads. Hence, the validation of the present FE formulation is made by neglecting the hygroscopic effect. In this regard, the numerical example considered by Kondaiah et al. [59] is solved using the present FE formulation. The plate dimensions and material properties
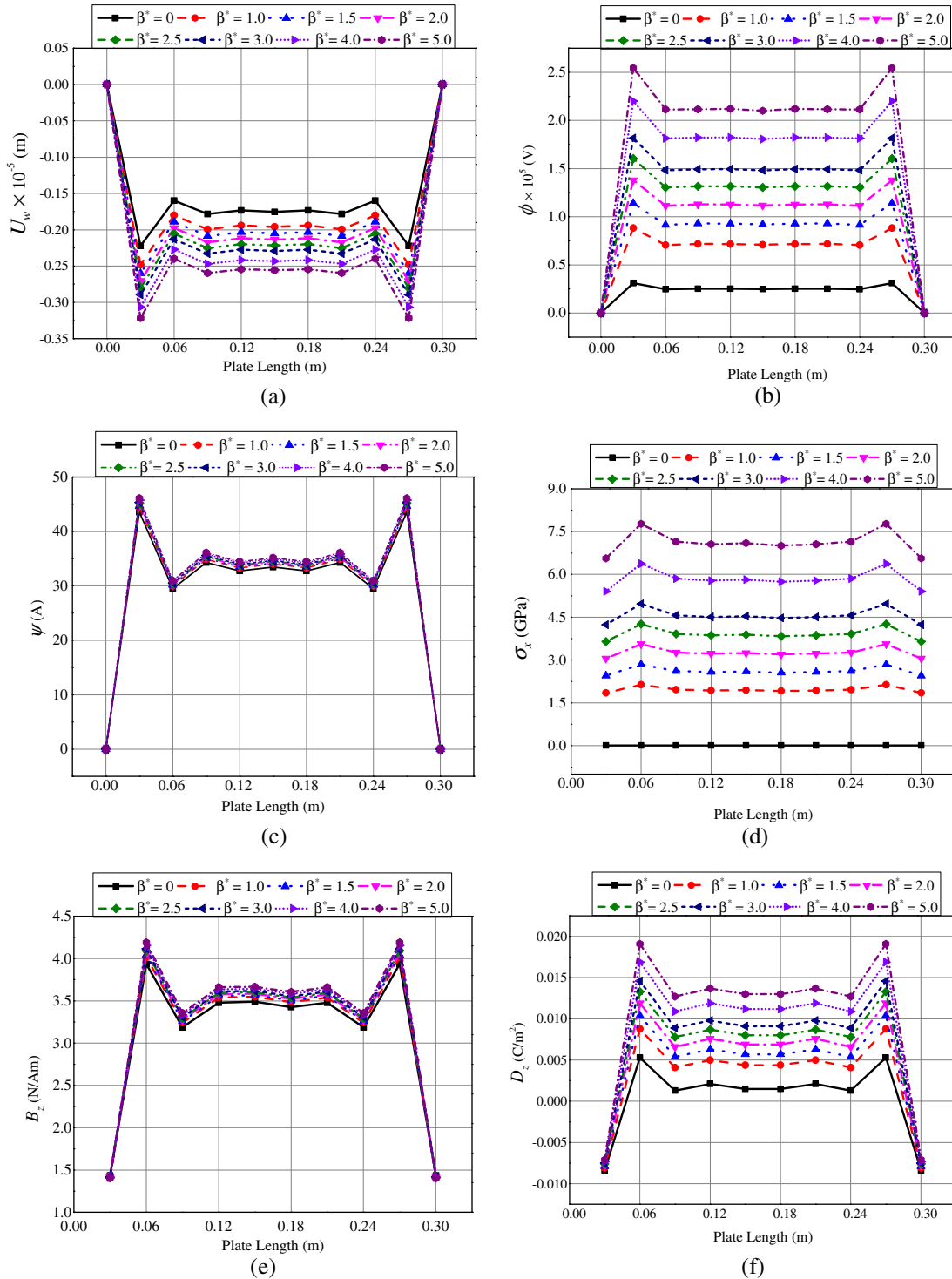

Fig. 12. Influence of β^* on (a) displacement component U_w (b) electric potential ϕ (c) magnetic potential ψ (d) normal stress σ_x (e) magnetic flux density B_z (f) electric displacement D_z.

of MEE plate remain unchanged. Fig. 3(a)–(f), indicate that for various boundary conditions, the results from the present FE formulation compare very well with Kondaiah et al. [59]. Hence, the correctness of FE formulation is justified. Further, the convergence study of the present FE model is depicted in Fig. 4 considering the electric potential ϕ of *FCFC* MEE plate. It can be observed from this figure that with the mesh size of $10 \times 10 \times 12$ elements, a good convergence of the present FE formulation can be achieved.
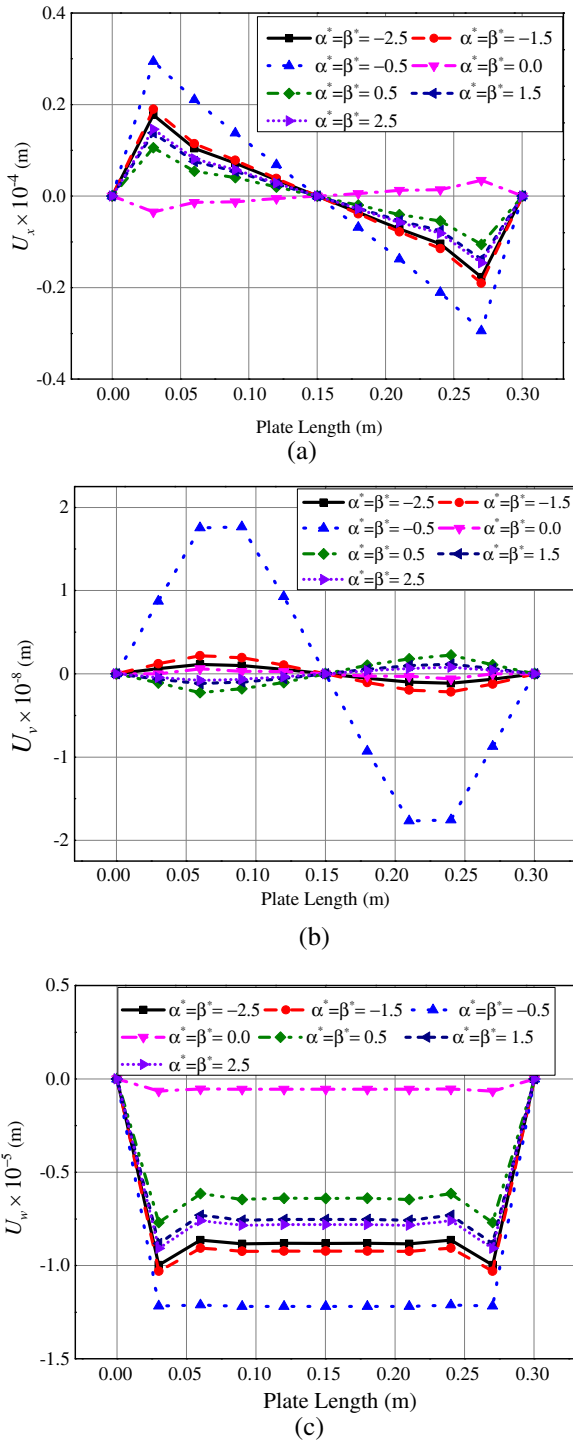
3.2. Effect of hygrothermal load

The effect of hygrothermal load on the static behavior of MEE plate with simply supported boundary conditions (*SSSS*) on all the edges of the plate (Fig. 2a) is considered for the analysis. For all the cases, the temperature rise is kept uniform (100 K), whereas the percentage moisture concentration change Δm is varied. The effect of hygrothermal load on variations of different parameters such as transverse displacement U_w, electric potential ϕ, magnetic potential ψ, normal stress σ_x, electric displacement D_x and magnetic flux density B_x of the *SSSS* MEE plate is plotted in Fig. 5(a)–(f), respectively. It is evident from these figures that with the increase in moisture concentration, the transverse displacement U_w, electric potential ϕ, magnetic potential ψ and normal stress σ_x increases, while a negligible influence of hygrothermal load is observed on the electric displacement component D_x and magnetic flux density component B_x. The MEE plate with *CCCC*, *CFFC* and *FCFC* boundary conditions also exhibit the same variation trend as the *SSSS* boundary condition. Hence, they are not presented here, for the sake of brevity.

3.3. Effect of temperature and moisture dependant elastic stiffness coefficients

The effect of temperature and moisture dependent elastic stiffness coefficients on the direct and derived quantities of the MEE plate is evaluated. The temperature and moisture dependent elastic stiffness coefficient C is given by [63]
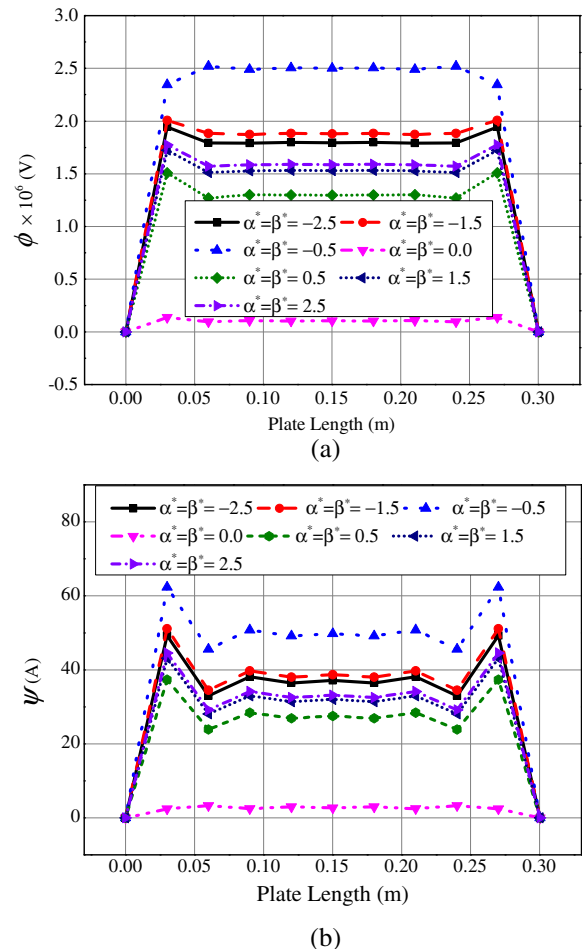

Fig. 13. Effect of empirical constants on (a) displacement component U_x (b) displacement component U_v (c) transverse displacement component U_w of *CCCC* MEE plate.

Fig. 14. Effect of empirical constants on (a) electric potential ϕ (b) magnetic potential ψ of *CCCC* MEE plate.

$$C = C_0(1 + \alpha^* \Delta T + \beta^* \Delta m) \tag{25}$$

where, α^* and β^* are called as empirical constants and C_0 corresponds to the temperature and moisture independent elastic coefficient. Further analysis assumes a uniform temperature rise $\Delta T = 100$ K and moisture concentration rise $\Delta m = 1\%$. In addition, emphasis has been placed to investigate the influence of different boundary conditions (*SSSS, CCCC, CFFC* and *FCFC*) on the static behavior of the MEE plate under hygrothermal loading.

3.3.1. Simply supported MEE plate (SSSS)

The boundary conditions corresponding to *SSSS* MEE plate is shown in Fig. 2(a). Fig. 6(a)–(c) illustrate the variation of displacement components along the length of the *SSSS* MEE plate for various temperature and moisture dependent empirical constants (α^*, β^*). It may be noticed from Fig. 6(a)–(c) that the MEE plate with empirical constants $\alpha^* = \beta^* = -0.5$ has a substantial influence on the displacements components U_x, U_v and U_w. It may be due to the fact that the elastic stiffness coefficient matrix [C] directly
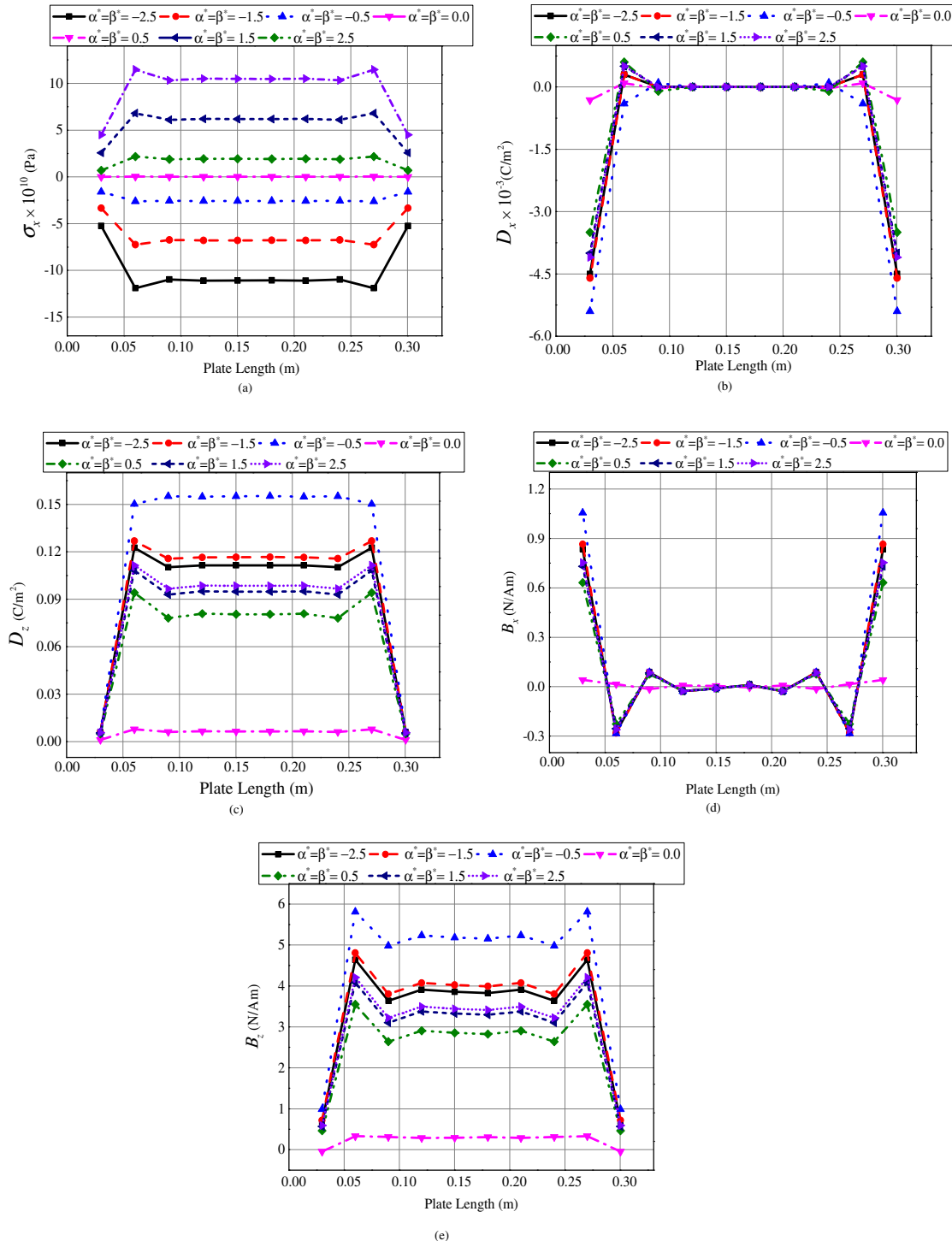

Fig. 15. Effect of empirical constants on (a) normal stress- σ_x (b) electric displacement components D_x (c) magnetic flux density components B_x of *CCCC* MEE plate.

affects the elastic stiffness matrix $[K_{tt}]$, hygroscopic load $\{F_{hy}\}$ and thermal load $\{F_{th}\}$ which in turn influences the $\{F_{eq}\}$ and $[K_{eq}]$. It may also be observed that for the empirical constants ranging from $-0.5 \leq \alpha^*, \beta^* \leq 0$, the influence of the temperature and moisture dependent elastic coefficients is more on the load vectors ($\{F_{hy}\}$ and $\{F_{th}\}$) as compared to the elastic stiffness matrix $[K_{tt}]$. In addition, with increase in negative empirical constants ($\alpha^*, \beta^* \geq -0.5$), the elastic stiffness matrix $[K_{tt}]$ improves in such a way that the value $[K_{eq}]^{-1}\{F_{eq}\}$ decreases. From Fig. 6(a) it may be noticed that for simply supported MEE plate, the maximum U_x is witnessed at

the edges of the plate. This may be due to unconstrained x-direction movement at the edges. A symmetric variation of the longitudinal displacement component U_v is noticed along the plate length. In comparison with the MEE plate with negative empirical constants, the hygrothermal loads have a minimal effect on U_v for different positive empirical constants. Meanwhile, at the centre of the plate, U_x and U_v are found to be zero. The transverse displacement component U_w remains almost constant along the plate length as illustrated in Fig. 6(c). Fig. 7(a) and (b) emphasise that $\alpha^* = \beta^* = -0.5$ has a predominant effect on the electric and magnetic potential, respectively. This is in accordance with the Eqs. (21.a) and (21.b), respectively. Also, it can be observed that the positive empirical constants increase the hygrothermo-magneto-electro-elasticity which in turn increases the electric and magnetic potentials of the MEE plate. Conversely, a reduction in the coupled behavior of MEE plate with respect to these potentials is observed with the higher negative empirical constants (say, $-2.5 \leq \alpha^*, \beta^* \leq -0.5$).

Fig. 8(a) demonstrates the distribution of the normal stress σ_x along the length of the MEE plate. It can be seen from this figure that the effect of hygrothermal loads on the normal stress σ_x is minimum when the MEE plate is considered to be made of temperature and moisture independent stiffness coefficients ($\alpha^* = \beta^* = 0.0$). For the corresponding positive and negative empirical constants, the MEE plate exhibits an equal but opposite sign of σ_x. In other words, the MEE plate experience tensile stress and compressive stress for positive and negative empirical constants, respectively. Since, the normal stresses σ_y and σ_z follows the sim-
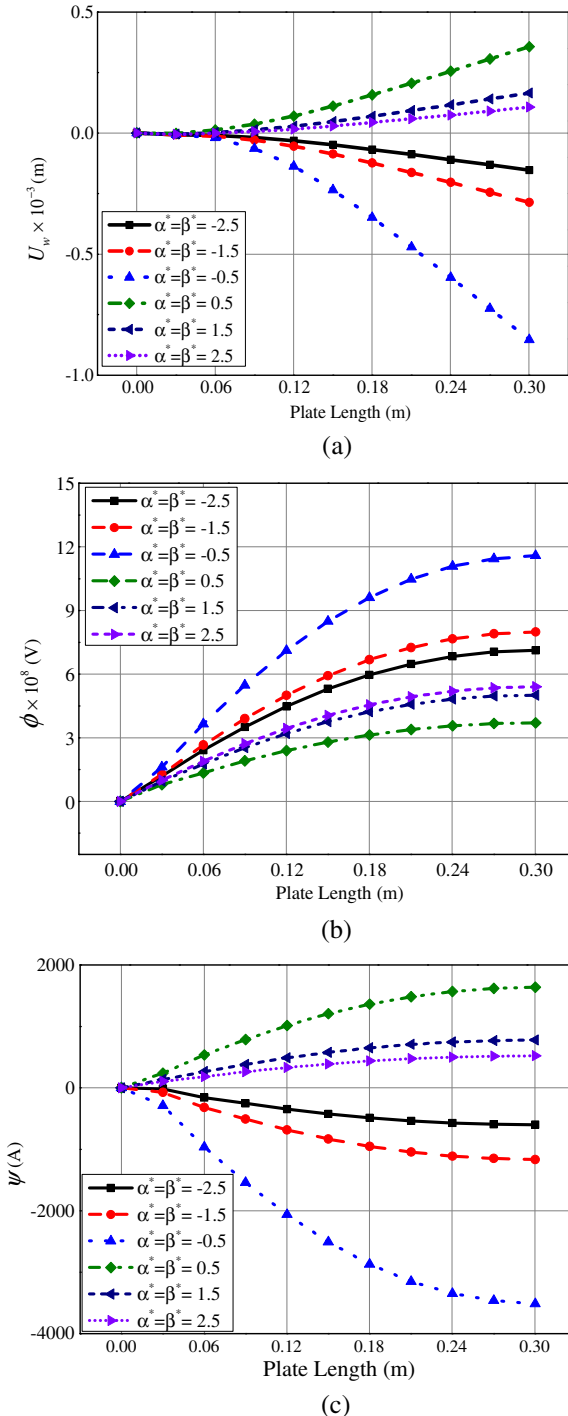

Fig. 16. Effect of empirical constants on (a) transverse displacement U_w (b) electric potential ϕ (c) magnetic potential ψ of *CFFC* MEE plate.
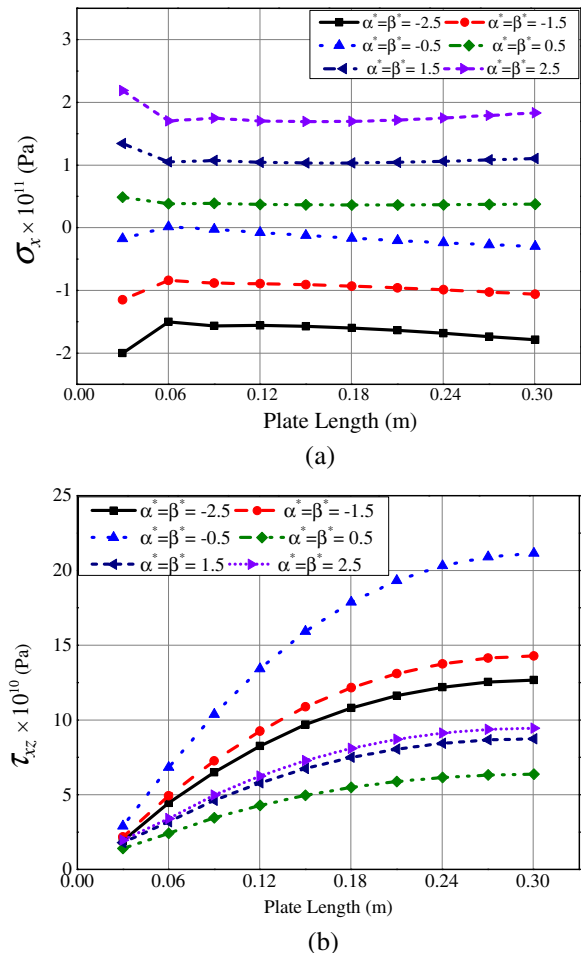

Fig. 17. Effect of empirical constants on (a) normal stress- σ_x (b) shear stress τ_{xz} of *CFFC* MEE plate.

ilar trend of variation as that of the σ_x, for the sake of brevity, the variation of σ_x alone is represented, here. Considering Fig. 8(b), at the midlength of the MEE plate the shear stress τ_{xy} is zero regardless of the empirical constants used. Before this point, the negative empirical constants and positive empirical constants of the MEE plate results in positive and negative value of τ_{xy}, respectively. In contrast, after this point the behavior of shear stress τ_{xy} is reversed. Furthermore, the shear stresses τ_{xz} and τ_{yz} displays a negligible variation with respect to empirical constants, whereas significant discrepancies are witnessed at the plate edges as illustrated in Fig. 8(c) and (d), respectively.

Fig. 9(a) depicts that the empirical constants have a negligible effect on the variation of electric displacement component D_x. However, for all the empirical constants, by imposing hygrothermal load the MEE plate experiences the maximum value of D_x at the plate edges. From Fig. 9(b), it can be noticed that D_z varies almost constant along the plate length and reaches the minimum value at the edges. In addition, it is deduced that the coupling effect on D_z is higher when the stiffness coefficients of the MEE plate corresponds to $\alpha^* = \beta^* = -0.5$ whereas, the MEE plate with
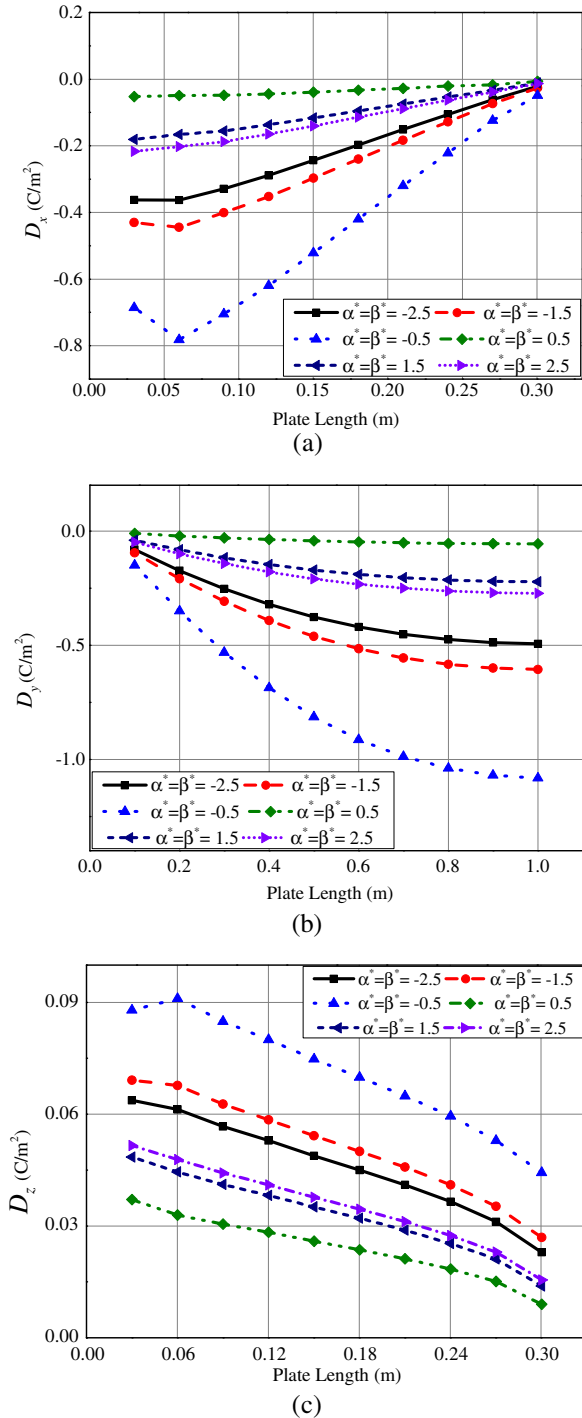

Fig. 18. Effect of empirical constants on electric displacement components (a) D_x (b) D_y (c) D_z of *CFFC* MEE plate.
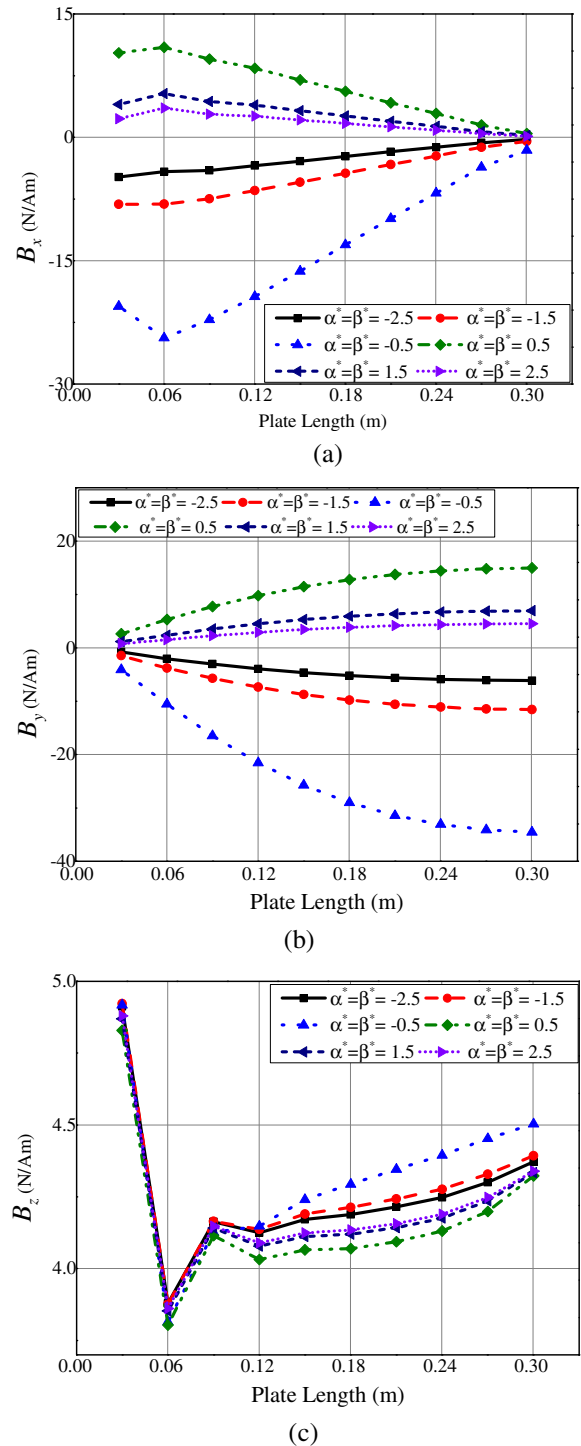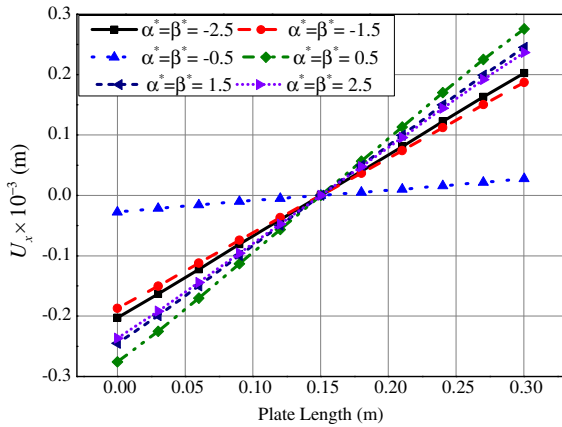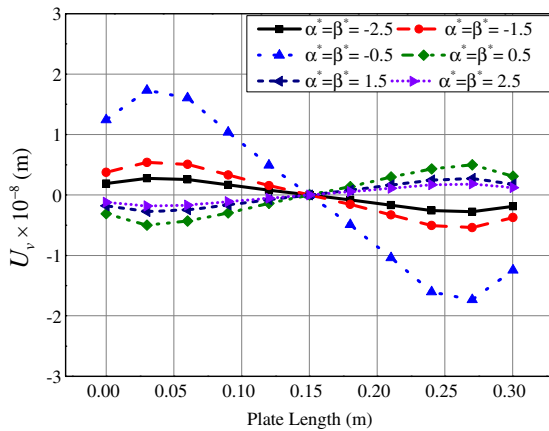

Fig. 19. Effect of empirical constants on magnetic flux density components (a) B_x (b) B_y (c) B_z of *CFFC* MEE plate.

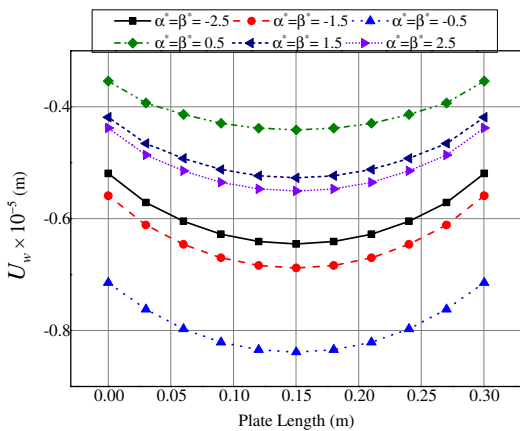$\alpha^* = \beta^* = 0.0$ yields minimal value of D_x and D_z when exposed to hygrothermal loads.

Fig. 10(a) and (b) display the variation of magnetic flux density components B_x and B_z, respectively. It can be pointed out from these figures that for the MEE plate with different empirical constants, the influence of hygrothermal loads on the magnetic flux density component B_z is significantly larger than B_x. This may be attributed to the higher value of piezomagnetic constants along z-direction. Meanwhile, the results suggest that the negative empirical constants have a predominant effect than the positive empirical constants.
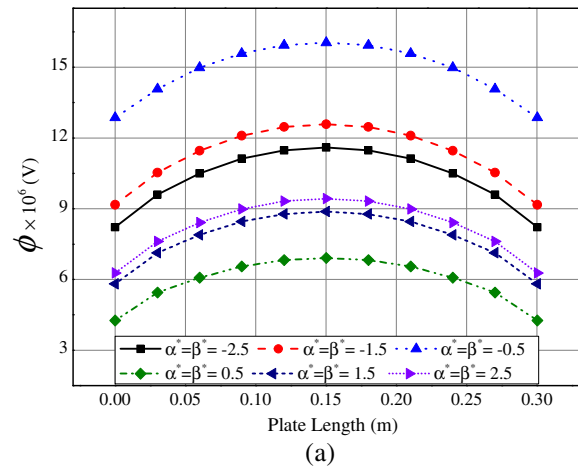
The dependency of the elastic stiffness coefficients on the temperature rise ΔT and moisture concentration rise Δm is studied by varying the empirical constants α^* and β^* individually. The value of β^* and α^* is nullified while evaluating the individual effect of α^* and β^*, respectively. Fig. 11(a)–(f) illustrate the influence of α^* on the displacement component U_w, electric potential ϕ, magnetic potential ψ, normal stress σ_x, magnetic flux density B_z and electric displacement D_z, respectively. Analogously, Fig. 12(a)–(f) depict the effect of β^*. It may be noticed from these figures that the influence of α^* on the displacement U_w is very small as compared to that of β^*. The variation trend is similar for the electric potential (ϕ) with respect to both α^* and β^*. Also, it is observed that the increase in the empirical constants α^* and β^* leads to negligible variation in the magnetic potential (ψ) along the plate length. An insignificant discrepancy with respect to the magnetic potential is noticed with the further increase in empirical constants. Since, the magnetic flux density B_z is directly influenced by the magnetic potential, this trend applies to the distribution of B_z also. Meanwhile, a substantial effect of both the empirical constants α^* and β^* on the variation of normal stress σ_x is observed from Figs. 11(d) and 12(d), respectively. In contrast to α^*, the predominant effect of β^* is witnessed on the electric displacement D_z.

3.3.2. Clamped MEE plate (CCCC)

The hygrothermo magneto-electro-elastic response of MEE plate with all sides clamped (CCCC) as depicted in Fig. 2(b) is analysed.

(a)

(b)

(c)

Fig. 20. Effect of empirical constants on (a) displacement component U_x (b) displacement component U_v (c) transverse displacement component U_w of *FCFC* MEE plate.
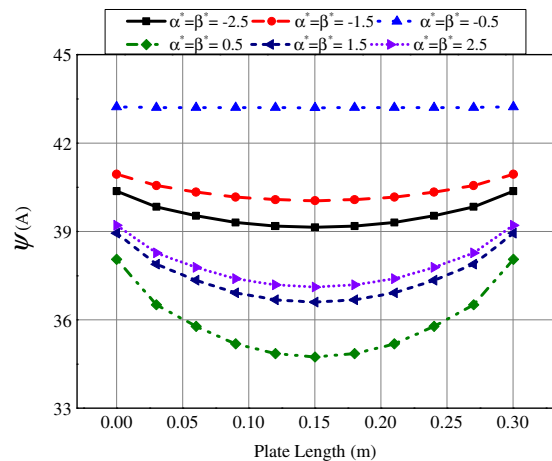

(a)

(b)

Fig. 21. Effect of empirical constants on (a) electric potential ϕ (b) magnetic potential ψ of *FCFC* MEE plate.

Fig. 13(a)–(c) demonstrate the plots of the displacement components U_x, U_v and U_w, respectively. A symmetrical variation of these components along the plate length can be observed. This is reasonable due to symmetric constraints along the MEE plate edges. Furthermore, Fig. 14(a) and (b) illustrate the effect of empirical constants on the variation of the electric and the magnetic potential of the *CCCC* MEE plate. Higher hyrgothermo-magneto-electro-elastic coupling with respect to $\alpha^* = \beta^* = -0.5$ leads to increased value of the potentials, similar to the *SSSS* MEE plate. Overall, it can be deduced that in this case also, the empirical constants $\alpha^* = \beta^* = -0.5$ exhibit a significant influence on the direct quantities of the system. When $\alpha^* = \beta^* = 0.0$, the MEE plate is subjected to a minimum stress. Further, irrespective of the empirical constants, the normal stress σ_x is maximum near the clamped edges and remains almost constant over the plate length as shown in Fig. 15(a). Because of multiphysical interactions, the electric displacement and magnetic flux densities are significantly affected by hygrothermal loading and the corresponding temperature an moisture dependant material properties. As seen in Fig. 15(b)–(e), the influence of temperature and moisture dependence is pronounced on the z-direction electric displacement and magnetic flux density components (D_z and B_z) than the x-direction components (D_x and B_x).

3.3.3. Adjacent side clamped MEE plate (CFFC)

In this case, a MEE plate with adjacent clamped edges (*CFFC*) as shown in Fig. 2(c) is considered for the analysis. Fig. 16(a) illustrates the variation of transverse displacement U_w. Due to asymmetric boundary conditions, the predominant effect of the hygrotherml loads can be observed at the free edge of the MEE plate. Hence, at the free edge the transverse displacement component U_w is maximum. Fig. 16(b) and (c) depict the electric potential and magnetic potential distribution, respectively. According to these figures, it may be noticed that higher positive empirical constants leads to increased electric potential, while the electric potential decreases as the negative empirical constants of temperature and moisture dependence increases. Fig. 16(c) depicts that with the increase in negative empirical constants the absolute values of the magnetic potential reduces, which makes the plot of magnetic potential shift towards the positive coordinate. In addition, as a result of higher hygrothermo-magneto-electro-elastic coupling at the free edge of the MEE plate, the electric potential and magnetic potential display a higher value. The magnitude of normal stress σ_x along the length of the *CFFC* MEE plate increases in response to the increasing empirical constants as displayed in Fig. 17(a). Further investigation reveals that the maximum normal stress σ_x is noticed at the clamped end, whereas the maximum shear stress τ_{xz} is observed at the free edge of the MEE plate as shown in Fig. 17(b).

Fig. 18(a)–(c) show the effect of empirical constants on the electric displacement components D_x, D_y and D_z, respectively. Unlike, the symmetric boundary conditions (*SSSS* and *CCCC*) of the MEE plate, a significant influence of empirical constants on the D_x and
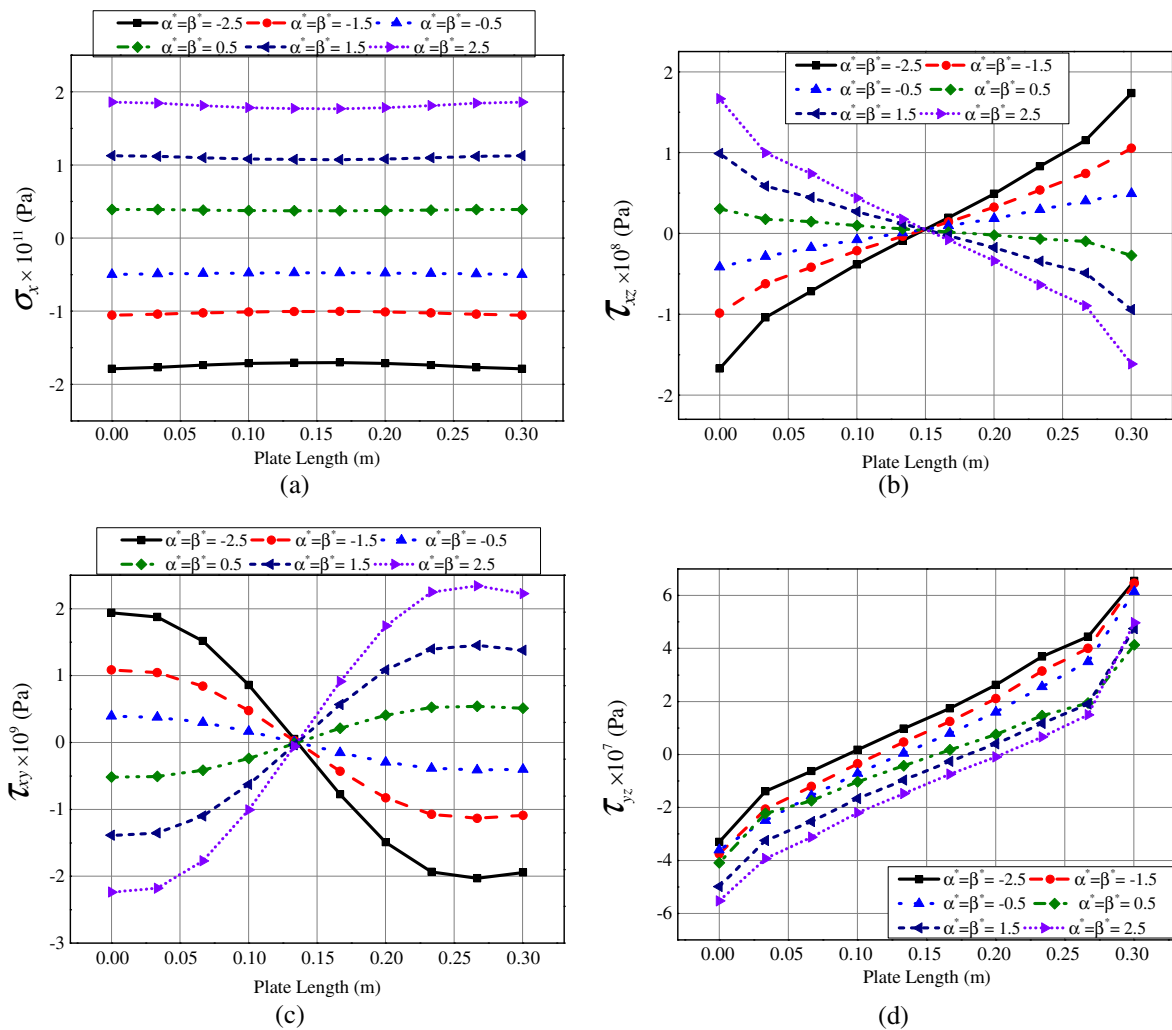

Fig. 22. Effect of empirical constants on (a) normal stress σ_x (b) shear stress τ_{xz} (c) shear stress τ_{xy} (d) shear stress τ_{yz} of *FCFC* MEE plate.

D_y are observed. This may be attributed to the fact that in comparison with symmetric boundary condition, the asymmetrical boundary conditions magnifies the effect of hygrothermal loads on the coupled response. Also, it is evident from these figures that a significant influence of empirical constants $\alpha^* = \beta^* = -0.5$ prevails. A linear variation of D_x and D_z along the plate length is witnessed with the maximum values at the clamped end, whereas D_y varies parabolically and reaches the maximum value at the free end.
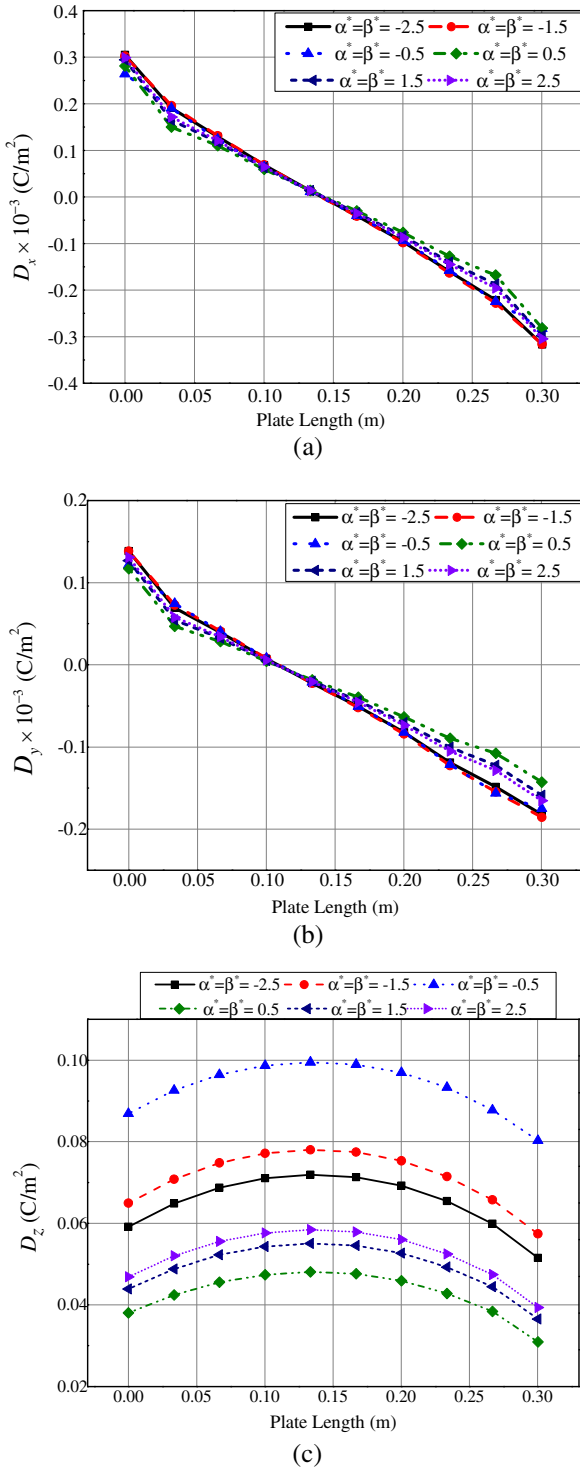
The distribution of magnetic flux density components B_x, B_y and B_z is illustrated in Fig. 19(a)–(c). It can be summarized from Fig. 19 (a) that in contrast to the MEE plate with positive empirical constants, the negative empirical constants results in an increasing trend of B_x along the plate length. Likewise, for all the empirical constants, the minimal value of B_x is found at the free end, whereas for B_y it is witnessed at the clamped edge.

3.3.4. Opposite side clamped MEE plate (FCFC)

The hygrothermal analysis of *FCFC* MEE plate has been carried out for the identical geometry used in the previous section. The

Fig. 23. Effect of empirical constants on electric displacement components (a) D_x (b) D_y (c) D_z of *FCFC* MEE plate.
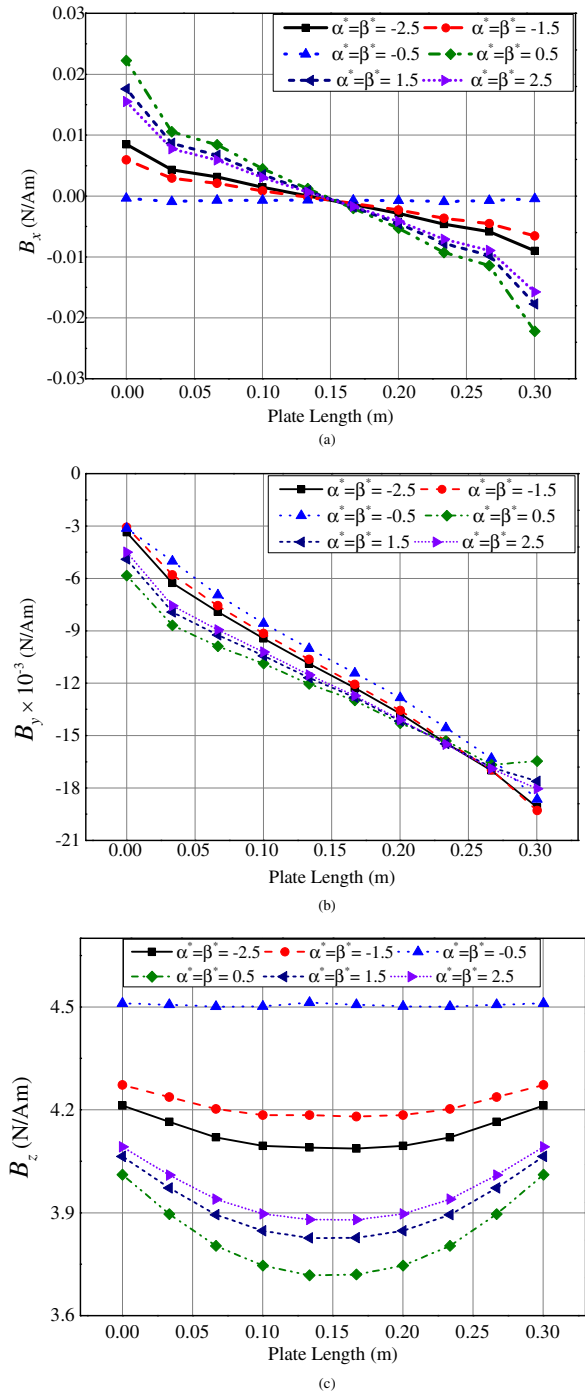

Fig. 24. Effect of empirical constants on magnetic flux density components (a) B_x (b) B_y (c) B_z of *FCFC* MEE plate.

Table 2
Effect of boundary conditions on the direct quantities of MEE plate.

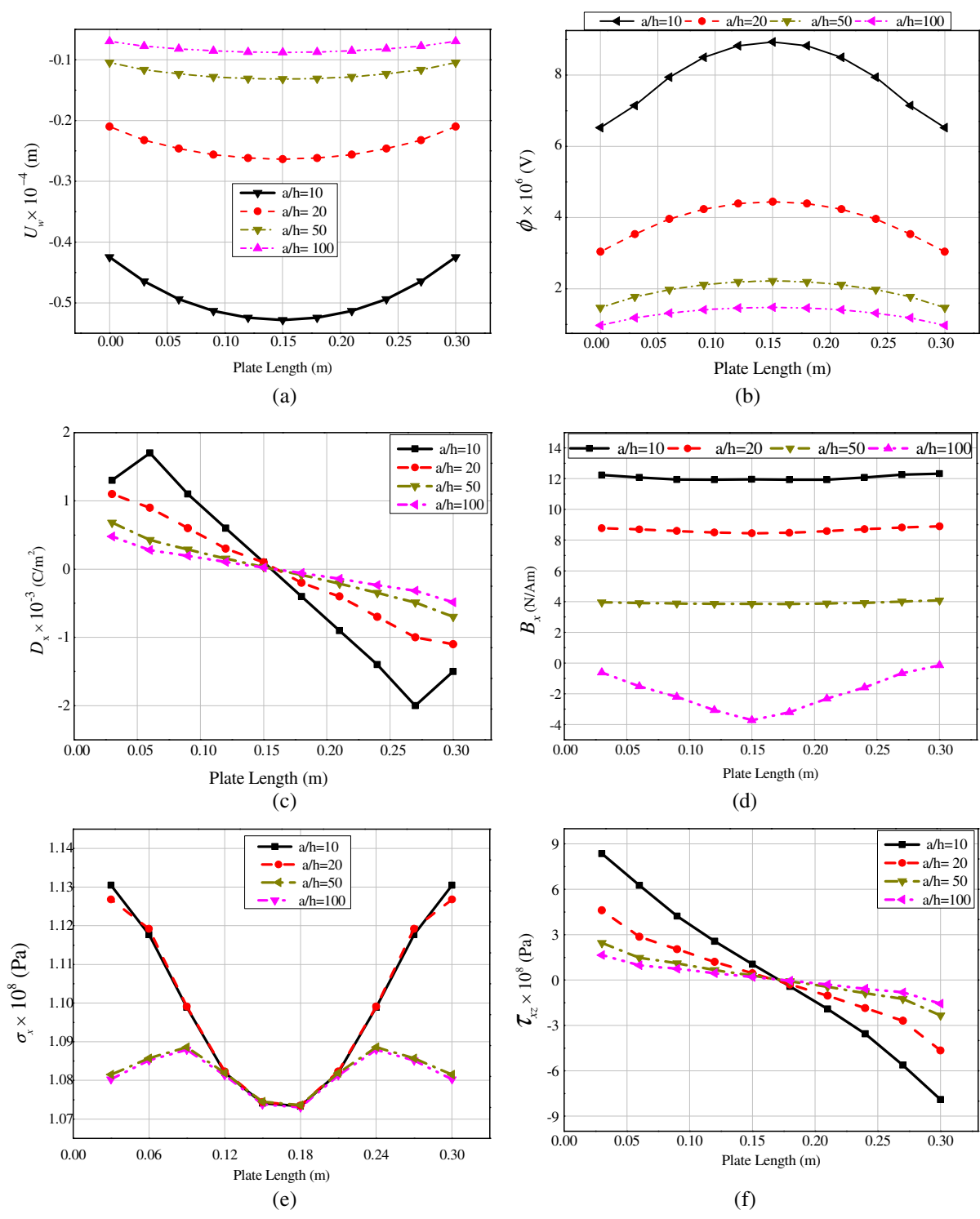| Parameter	CCCC	SSSS	CFFC	FCFC
U_x (m)	0.013792×10^{-3}	-0.15973×10^{-3}	0.2855×10^{-3}	0.245204×10^{-3}
U_v (m)	0.117415×10^{-8}	-0.10567×10^{-9}	0.1927×10^{-3}	0.271777×10^{-8}
U_w (m)	-0.88173×10^{-5}	-0.53245×10^{-5}	6.9×10^{-5}	-0.5271×10^{-5}
ϕ (V)	1.723439×10^{6}	6.607276×10^{5}	5.0142×10^{8}	8.87785×10^{5}
ψ (A)	43.13319	50.77091	781.2889	38.94086

Fig. 25. Effect of aspect ratio a/h on (a) displacement component U_w (b) electric potential ϕ (c) electric displacement D_x (d) magnetic flux density component B_z (e) normal stress σ_x (f) shear stress component τ_{xz}.

edges adjoining the mid-length are set a free, while the edges on either side of the mid-length are clamped. This arrangement is schematically represented in Fig. 2(d). The displacement components U_x, U_v and U_w for the *FCFC* MEE plate are shown in Fig. 20 (a)–(c), respectively. It is noticed from Fig. 20(a) that unlike remaining boundary condition, the MEE plate with empirical constants of $\alpha^* = \beta^* = -0.5$ has a minute influence on U_x. The variation of the electric potential and magnetic potential due to multiphysics interaction of hygrothermal loading is illustrated in Fig. 21 (a) and (b), respectively. The positive empirical constants is directly proportional to both the potentials (ϕ and ψ), whereas the negative empirical constants have an adverse effect. Further investigation reveals that at the midspan of the MEE plate, the hygrothermal loads generate the maximum and minimum values of electric potential and magnetic potential, respectively. The results depicted in Fig. 22(a) indicate that the absolute value of the normal stress σ_x along the plate length increases with the increase in both positive and negative empirical constants. For all the empirical constants, the shear stresses τ_{xy} and τ_{xz} vary symmetrically along the plate length as illustrated in Fig. 22 (b) and (c), respectively. The shear stress component τ_{yz} varies linearly along the plate length (Fig. 22(e)). Fig. 23(a)–(c) demonstrate the effect of empirical constants on the electric displacement components D_x, D_y and D_z, respectively. An insignificant effect of the empirical constants may be noticed on the variations of D_x and D_y along the plate length, while a significant effect is witnessed for D_z. Contrary to *CFFC* MEE plate, it is noticed from Fig. 24(a) that $\alpha^* = \beta^* = -0.5$ has a least influence on the magnetic flux density component B_x. Meanwhile, for all the empirical constants the B_x varies linearly along the plate length and reaches the maximum values at the free edges of the *FCFC* MEE plate. Fig. 24(b) shows the variation of B_y along the plate length of the *FCFC* MEE plate. The distribution of the magnetic flux density component B_z is dominated by the empirical constants $\alpha^* = \beta^* = -0.5$ as illustrated in Fig. 24(c).

A comparative study of the effect of boundary conditions on the maximum values of the direct quantities is encapsulated in Table 2. It can be inferred that the *CFFC* boundary condition of the MEE plate results in a higher magnitude of displacements and potentials.

3.4. Effect of a/h ratio

In this section, the effect of aspect ratio (a/h) on some of the parameters of a *FCFC* MEE plate is evaluated. A uniform hygrothermal load of $\Delta T = 100$ K, $\Delta m = 1\%$ moisture concentration change and $\alpha^* = \beta^* = 1.0$ is assumed for the analysis. Fig. 25(a)–(f) demonstrate the variations of transverse displacement U_w, electric potential, electric displacement D_x, magnetic flux density B_x, normal stress σ_x and shear stress τ_{xz}, respectively. It may be noticed from these figures that a predominant effect of the lower aspect ratio ($a/h = 10$) prevails on the hygrothermo-magneto-electro-elastic response of the MEE plates.

4. Conclusions

In this paper, the effect of hygrothermal loading on the multiphysics response of magneto-electro-elastic (MEE) plate is investigated using finite element (FE) methods. A FE element formulation is derived with the aid of the principle of total potential energy and linear coupled constitutive equations of MEE material. The numerical results suggest that the direct quantities and stresses vary proportionally to the applied hygrothermal loads. However, a negligible influence of hygrothermal loads is reported on the electric displacement components (D_x and D_y) and magnetic flux den-

sity components (B_x and B_y). The empirical constants $\alpha^* = \beta^* = -0.5$ has a significant influence on the displacement components and potentials of the MEE plate. The normal stress components vary accordingly with the empirical constants, while the empirical constants have a negligible effect on the shear stress components (τ_{xz} and τ_{yz}), electric displacement components (D_x and D_y) and magnetic flux density components (B_x and B_y). Among all the boundary conditions considered, a distinguishable effect of empirical constants on the D_x, D_y, B_x and B_y is observed only for *CFFC* MEE plate. In addition, *CFFC* boundary condition has a predominant effect on the direct quantities. Finally, the investigation of the effect of aspect ratio reveals that lower aspect ratio (thick plates) has a significant effect on the static parameters of MEE plate. It is believed that the current results reveal the possible interactions of different physical fields on the structural behavior of smart systems.

References

[1] Nan CW. Magnetoelectric effect in composites of piezoelectric and piezomagnetic phases. Phys Rev B 1992;50:6082.
[2] Tounsi A, Houari MSA, Benyoucef S. A refined trigonometric shear deformation theory for thermoelastic bending of functionally graded sandwich plates. Aerosp Sci Technol 2013;24(1):209–20.
[3] Zenkour AM, Alghamdi NA. Thermoelastic bending analysis of functionally graded sandwich plates. J Mater Sci 2008;43(8):2574–89.
[4] Houari MSA, Tounsi A, Bég OA. Thermoelastic bending analysis of functionally graded sandwich plates using a new higher order shear and normal deformation theory. Int J Mech Sci 2013;76:102–11.
[5] Bourada M, Tounsi A, Houari MSA, Bedia EAA. A new four-variable refined plate theory for thermal buckling analysis of functionally graded sandwich plates. J Sandw Struct Mater 2012;14(1):5–33.
[6] Wang HM. Thermally induced piezothermoelastic fields of a smart sandwich cylindrical structure with a functionally graded interlayer. J Therm Stresses 2014;37(5):585–603.
[7] Saadatfar M, Rastgoo A. Stress in piezoelectric hollow sphere with thermal gradient. J Mech Sci Technol 2008;22(8):1460.
[8] Saadatfar M, Razavi AS. Piezoelectric hollow cylinder with thermal gradient. J Mech Sci Technol 2009;23(1):45–53.
[9] Saadatfar M, Khafri AM. On the magneto-thermo-elastic behavior of a functionally graded cylindrical shell with pyroelectric layers featuring interlaminar bonding imperfections rested in an elastic foundation. J Solid Mech 2015;7(3):344–63.
[10] Saadatfar M, Khafri AM. Electromagnetothermoelastic behavior of a rotating imperfect hybrid functionally graded hollow cylinder resting on an elastic foundation. Smart Struct Syst 2015;15(6):1411–37.
[11] Saadatfar M, Khafri AM. Thermoelastic analysis of a rotating functionally graded cylindrical shell with functionally graded sensor and actuator layers on an elastic foundation placed in a constant magnetic field. J Intell Mater Syst Struct 2016;27(4):512–27.
[12] Alibeigloo A, Nouri V. Static analysis of functionally graded cylindrical shell with piezoelectric layers using differential quadrature method. Compos Struct 2010;92(8):1775–85.
[13] Alibeigloo A. Static analysis of a functionally graded cylindrical shell with piezoelectric layers as sensor and actuator. Smart Mater Struct 2009;18(6):065004.
[14] Alibeigloo A. Thermoelastic solution for static deformations of functionally graded cylindrical shell bonded to thin piezoelectric layers. Compos Struct 2011;93(2):961–72.
[15] Alashti RA, Khorsand M. Three-dimensional thermo-elastic analysis of a functionally graded cylindrical shell with piezoelectric layers by differential quadrature method. Int J Pres Ves Pip 2011;88(5):167–80.
[16] Alashti RA, Khorsand M. Three-dimensional dynamo-thermo-elastic analysis of a functionally graded cylindrical shell with piezoelectric layers by DQ-FD coupled. Int J Pres Ves Pip 2012;96:49–67.
[17] Brischetto S. Hygrothermoelastic analysis of multilayered composite and sandwich shells. J Sandw Struct Mater 2013;15(2):168–202.
[18] Natarajan S, Deogekar PS, Manickam G, Belouettar S. Hygrothermal effects on the free vibration and buckling of laminated composites with cutouts. Compos Struct 2014;108(1):848–55.
[19] Parhi A, Singh BN. Stochastic response of laminated composite shell panel in hygrothermal environment. Mech Based Des Struc 2014;42(4):454–82.
[20] Alzahrani EO, Zenkour AM, Sobhy M. Small scale effect on hygro-thermo-mechanical bending of nanoplates embedded in an elastic medium. Compos Struct 2013;105:163–72.
[21] Mahapatra TR, Panda SK. Nonlinear free vibration analysis of laminated composite spherical shell panel under elevated hygrothermal environment: A micromechanical approach. Aerosp Sci Technol 2016;49:276–88.
[22] Zidi M, Tounsi A, Houari MSA, Bedia EAA, Anwar Beg O. Bending analysis of FGM plates under hygro-thermo-mechanical loading using a four variable refined plate theory. Aerosp Sci Technol 2014;34:24–34.

[23] Saadatfar M, Khafri AM. Hygrothermal analysis of a rotating smart exponentially graded cylindrical shell with imperfect bonding supported by an elastic foundation. Aerosp Sci Technol 2015;43:37–50.

[24] Saadatfar M, Khafri AM. On the behavior of a rotating functionally graded hybrid cylindrical shell with imperfect bonding subjected to hygrothermal condition. J Therm Stresses 2015;38(8):854–81.

[25] Saadatfar M. Effect of multiphysics conditions on the behavior of an exponentially graded smart cylindrical shell with imperfect bonding. Meccanica 2015;50(8):2135–52.

[26] Smittakorn W, Heyliger PR. An adaptive wood composite: theory. Wood Fiber Sci 2001;33(4):595–608.

[27] Smittakorn W, Heyliger PR. Adaptive wood composite: experiment. J Struct Eng 2003;129:699–702.

[28] Smittakorn W, Heyliger PR. A discrete-layer model of laminated hygrothermopiezoelectric plates. Mech Compos Mater Struct 2000;7:79–104.

[29] Raja S, Sinha PK, Raja S, Dwarakanathan D, Sinha PK, Prathap G. Bending behavior of piezo-hygrothermo-elastic smart laminated composite flat and curved plates with active control. J Reinf Plast Compos 2004;23:265–90.

[30] Raja S, Sinha PK, Prathap G, Dwarakanathan D. Influence of active stiffening on dynamic behavior of piezo-hygro-thermo-elastic composite plates and shells. J Sound Vib 2004;278:257–83.

[31] Kerur SB, Ghosh A. Geometrically Non-Linear Bending Analysis of Piezoelectric Fiber-Reinforced Composite (MFC/AFC) Cross-Ply Plate under Hygrothermal Environment. J Therm Stresses 2013;36(12):1255–82.

[32] Zenkour AM. Hygrothermoelastic responses of inhomogeneous piezoelectric and exponentially graded cylinders. Int J Press Vessels Pip 2014;119:8–18.

[33] Pan E. Exact solution for simply supported and multilayered magneto-electro-elastic plates. J Appl Mech-T ASME 2001;68:608–18.

[34] Ramirez F, Heyliger PR, Pan E. Free vibration response of two-dimensional magneto-electro-elastic laminated plates. J Sound Vib 2006;292:626–44.

[35] Chen J, Chen H, Pan E, Heyliger PR. Modal analysis of magneto-electro-elastic plates using the state-vector approach. J Sound Vib 2007;304:722–34.

[36] Milazzo A. Refined equivalent single layer formulations and finite elements for smart laminates free vibrations. Compos Part B Eng 2014;61:238–53.

[37] Wang Y, Xu R, Ding H, Chen J. Three dimensional exact solutions for free vibrations of simply supported magneto-electro-elastic cylindrical panels. Int J Eng Sci 2010;48:1778–96.

[38] Tsai YH, Wu CP. Dynamic responses of functionally graded magneto-electro-elastic shells with open circuit surface conditions. Int J Eng Sci 2008;46:843–57.

[39] Xin L, Hu Z. Free vibration of simply supported and multilayered magneto-electro-elastic plates. Compos Struct 2015;121:344–50.

[40] Kattimani SC, Ray MC. Smart damping of geometrically nonlinear vibrations of magneto-electro-elastic plates. Compos Struct 2014;14:51–63.

[41] Kattimani SC, Ray MC. Active control of large amplitude vibrations of smart magneto-electro-elastic doubly curved shells. Int J Mech Mater Des 2014;10(4):351–78.

[42] Kattimani SC, Ray MC. Control of geometrically nonlinear vibrations of functionally graded magneto-electro-elastic plates. Int J Mech Sci 2015;99:154–67.

[43] Lage RG, Soares CMM, Soares CAM, Reddy JN. Layerwise partial mixed finite element analysis of magneto-electro-elastic plates. Comput Struct 2004;82:1293–301.

[44] Pan E, Han F. Exact solutions for functionally graded and layered magneto-electro-elastic plates. Int J Eng Sci 2005;43:321–39.

[45] Bhangale RK, Ganesan N. Static analysis of simply supported functionally graded and layered magneto-electro-elastic plates. Int J Solids Struct 2006;43(10):3230–53.

[46] Carrera E, Di Gifico M, Nali P, Brischetto S. Refined multilayered plate elements for coupled magneto-electro-elastic analysis. Multidiscipline Model Mater Struct 2009;5(2):119–38.

[47] Wu CP, Tsai YH. Static behavior of functionally graded magneto-electro-elastic shells under electric displacement and magnetic flux. Int J Eng Sci 2007;45:744–69.

[48] Huang DJ, Ding HJ, Chen WQ. Analytical solution for functionally graded magneto-electro-elastic plane beams. Int J Eng Sci 2007;45:467–85.

[49] Alaimo A, Benedetti I, Milazzo A. A finite element formulation for large deflection of multilayered magneto-electro-elastic plates. Compos Struct 2014;107:643–53.

[50] Li YS. Buckling analysis of magnetoelectroelastic plate resting on Pasternak elastic foundation. Mech Res Commun 2014;56:104–14.

[51] Kumaravel A, Ganesan N, Sethuraman R. Buckling and vibration analysis of layered and multiphase magnetoelectroelastic beam under thermal loading. Multidiscipline Model Mater Struct 2010;6(4):475–92.

[52] Lang Z, Xuewu L. Buckling and vibration analysis of functionally graded magneto-electro-thermo-elastic circular cylindrical shells. Appl Math Model 2013;37:2279–92.

[53] Carrera E, Brischetto S, Fagiano C, Nali P. Mixed multilayered plate elements for coupled magneto-electro-elastic analysis. Multidiscipline Model Mater Struct 2009;5(3):251–6.

[54] Milazzo A. Layer-wise and equivalent single layer models for smart multilayered plates. Compos Part B Eng 2014;67:62–75.

[55] Benedetti I, Milazzo A. Advanced models for smart multilayered plates based on Reissner Mixed Variational Theorem. Compos Part B Eng 2017;119:215–29.

[56] Sunar M, Al-Garni AZ, Ali MH, Kahraman R. Finite element modeling of thermopiezomagnetic smart structures. AIAA J 2002;40:1845–51.

[57] Ootao Y, Tanigawa Y. Transient analysis of multilayered magneto-electro-thermoelastic strip due to non uniform heat supply. Compos Struct 2005;68:471–80.

[58] Kumaravel A, Ganesan N, Sethuraman R. Steady-state analysis of a three-layered electro-magneto-elastic strip in a thermal environment. Smart Mater Struct 2007;16:282–95.

[59] Kondaiah P, Shankar K, Ganesan N. Pyroelectric and pyromagnetic effects on behavior of magneto-electro-elastic plate. Coupled Syst Mech 2013;2:1–22.

[60] Kondaiah P, Shankar K, Ganesan N. Studies on magneto-electro-elastic cantilever beam under thermal environment. Coupled Syst Mech 2012;1(2):205–17.

[61] Vinyas M, Kattimani SC. Static studies of stepped functionally graded magneto-electro-elastic beams subjected to different thermal loads. Compos Struct 2017;163:216–37.

[62] Vinyas M, Kattimani SC. A finite element based assessment of static behavior of multiphase magneto-electro-elastic beams under different thermal loading. Struct. Eng. Mech. 2017;62(5):519–35.

[63] Akbarzadeh AH, Chen ZT. Magnetoelectroelastic behavior of rotating cylinders resting on an elastic foundation under hygrothermal loading. Smart Mater Struct 2012;2:125013.

[64] Akbarzadeh AH, Chen ZT. Hygrothermal stresses in one dimensional functionally graded piezoelectric media in constant magnetic field. Compos Struct 2013;97:317–31.

[65] Saadatfar M, Khafri AM. Hygrothermomagnetoelectroelastic analysis of a functionally graded magnetoelectroelastic hollow sphere resting on an elastic foundation. Smart Mater Struct 2014;23:035004.

[66] Akbarzadeh AH, Pasini D. Multiphysics of multilayered and functionally graded cylinders under prescribed hygrothermomagnetoelectromechanical loading. J Appl Mech-T ASME 2014;81:041018.